3.C

Nuclear Physics **A217** (1973) 29—70; © *North-Holland Publishing Co., Amsterdam*

SPECTROSCOPIC FACTORS FROM RADIATIVE CAPTURE REACTIONS

C. ROLFS †

University of Toronto, Toronto, Canada ††

Received 3 September 1973

Abstract: The non-resonant γ-ray yield in radiative capture reactions is known to arise from a direct-capture process. Previous studies of this process in several light nuclei have been mainly concerned with astrophysical aspects. The present work demonstrates that this process can be in addition a useful tool in nuclear spectroscopy. The process selects states in the final nucleus which have parentage in the ground state of the target nucleus. The observed γ-ray angular distributions are characterized by the orbital angular momenta of the final states and the observed total cross sections reveal, when compared with model calculations, the spectroscopic factors for the final states. These features are similar to results derived from stripping reactions. The direct capture mechanism (electromagnetic interaction) is amenable to exact calculations in contrast to the more complex stripping reaction mechanism. The results for proton capture by ^{16}O and ^{17}O targets will be compared with available stripping data as well as shell-model calculations.

E NUCLEAR REACTIONS ^{16}O(p,γ), E = 0.3–3.1 MeV; measured $\sigma(E_p)$, E_γ, I_γ, $I_\gamma(\theta)$. ^{17}O(p,γ), E = 0.3–1.9 MeV; measured $\sigma(E_p)$, E_γ, I_γ, $I_\gamma(\theta)$. ^{17}F and ^{18}F levels deduced I, J, γ-branching, spectroscopic factors. Natural, depleted and enriched targets.

1. Introduction

In many light nuclei the cross section for the radiative capture of protons [refs. [1–13])], deuterons [ref. [47]) and references therein], ^{3}He [ref. [14])] and ^{4}He [ref. [15])] has been observed ††† to consist of a background, slowly varying with beam energy, upon which the various known resonances in the reaction are superposed. The total cross section for this smooth background is, in the case of proton capture, characteristically of the order of 1 to 10 μb. This smooth background has been identified [16–24]) as an extra-nuclear channel phenomenon, since the matrix elements of the process are dominated by the contributions from the channel rather than, as usually is the case, by the nuclear interior (subsect. 2.2). These reactions are therefore necessarily non-resonant since they do not involve the formation of a compound state. For this reason they have been designated as direct capture (single-step) reactions.

Previous experimental and theoretical studies of this process, for several light nuclei, have been mainly concerned with the astrophysical aspects [54, 55]).

† Present address: California Institute of Technology, Kellogg Rad. Lab., Pasadena, California, 91109.

†† Work partially supported by National Research Council, Canada.

††† The direct capture of neutrons has been described in the literature [24, 25, 51]).

The direct capture process represents a transition for the projectile from an initial continuum state (Coulomb distorted plane wave) to a final state (standing wave with characteristic orbital angular momentum l_f) via interaction with the electromagnetic field. The reaction selects those projectiles from the appropriate partial waves with orbital angular momenta l_i which can jump into final orbits (l_f) by the emission of γ-radiation of multipolarity L. Such a process can be expected for final states which have parentage in the ground state of the target nucleus. Since the continuum states (i.e. phase shifts) can be determined from elastic scattering data and the electromagnetic interaction Hamiltonian is well-known, comparisons of the experimental and theoretical cross sections can provide the spectroscopic factors for the final states. The direct capture reaction has this feature in common with other direct reactions, e.g. stripping reactions, but has the advantage that (i) the process represents basically a two-body problem rather than a three-body problem and (ii) the process is induced by the well-known electromagnetic interaction rather than the less well-known nuclear force. In addition, the weakness of the electromagnetic forces, relative to nuclear forces, allows a first-order time dependent perturbation theory to be used in computing the cross sections.

The present work describes a detailed experimental and theoretical study of the direct capture process of protons by ^{16}O and ^{17}O target nuclei. The theoretical calculations are based on a simple two-body model (sect. 2). The formalism for this model has been obtained from Christy and Duck [16]), Tombrello and Parker [17]) and Donnelly [20]). Expressions for the γ-ray angular distributions for the direct capture and secondary transitions are derived in the appendix. Preliminary results of these studies have been reported [48]) and are now superseded by the present work.

2. Theoretical considerations

2.1. GENERAL EXPRESSIONS FOR THE CAPTURE CROSS SECTIONS

The direct radiative capture reaction A(x, γ)B, representing the capture of particle x (mass M_1, charge Z_1) by a target A (mass M_2, charge Z_2) to form a final state B of the combined system with the emission of γ-radiation of energy E_γ, can be described with the aid of the Hamiltonian

$$H = H_0 + H_{\text{int}}, \tag{1}$$

where H_0 contains the Hamiltonian of the A+x (or B) system and the free electromagnetic field, and H_{int} represents the usual Hamiltonian for the interaction between the particles and the electromagnetic field. One can treat H_{int} as a small perturbation on H_0. The validity of this approximation is evidenced by the small cross sections involved in direct capture reactions ($\approx \mu$b) compared to cross sections ($\approx$ b) in the case of elastic scattering. Using first-order time dependent perturbation theory, Tombrello and Parker [17]) have calculated the differential cross section for direct

radiative capture from continuum to bound states:

$$\frac{d\sigma}{d\Omega} = \frac{E_\gamma}{2\pi\hbar^2 c v_i (2j_p+1)(2j_t+1)} \sum_{m_i m_f P} |\langle f, m_f|H_{int}|i, m_i\rangle|^2, \tag{2}$$

where j_p and j_t are the spins of the projectile and target, respectively, and P is the circular polarization of the γ-radiation ($P = \pm 1$), v_i is the relative velocity in the asymptotic region of the projectile and target nucleus, i and f refer to wave functions describing the continuum and bound states of the combined system B.

The electromagnetic interaction, in the case of E1 radiation, is given [17,19,63]) by

$$H_{int}(E1) = \sum_m (-i)(\tfrac{4}{3}\pi)^{\frac{1}{2}} P e \frac{E_\gamma}{\hbar c} \frac{M_1 M_2}{M_1+M_2} \left(\frac{Z_1}{M_1} - \frac{Z_2}{M_2}\right) D^{(1)*}_{mP}(\varphi_\gamma, \vartheta_\gamma, 0) \mathcal{O}_{E1}(r) \mathcal{Y}_1^{m*}(\vartheta, \varphi), \tag{3}$$

where m is the magnetic quantum number of the radiation, e is the electric charge and $D^{(1)*}_{mP}(\varphi_\gamma, \vartheta_\gamma, 0)$ are elements of the rotation matrix for $L = 1$. The angles $(\vartheta_\gamma, \varphi_\gamma)$ specify the direction of the emitted γ-radiation with respect to the beam direction and (r, ϑ, φ) are the coordinates of the projectile in the centre-of-mass frame. The effect of the nuclear recoil is taken into account through the reduced mass and the factor $(Z_1/M_1 - Z_2/M_2)$. In the long wavelength approximation, i.e. for $\rho = k_\gamma r \ll 1$, the exact radial part [19])

$$\mathcal{O}_{E1}(r) = [(\rho^2-2)\sin\rho + 2\rho\cos\rho]3r/\rho^3 \tag{4}$$

of the E1 multipole operator approaches the usual r. It should be noted here that in calculating direct capture cross sections for low beam energies ($E_p \leqq 300$ keV) the radial integral (subsect. 2.2) has to be taken as far as 400 fm so that the condition $k_\gamma r \ll 1$ is not always fulfilled. Expressions for M1 and E2 interaction Hamiltonians can be found in the literature [17,19,63]).

In this model [16,17,20]) it is assumed that the many-nucleon problem can be approximated by a two-body problem, in which the target nucleus A as well as the projectile x are treated as inert cores, i.e. as single particles. The systems are then described, both in the initial (continuum) and final (bound) states as a valence nucleon (projectile) interacting with the target nucleus A.

The initial-state wave function for the projectile incident along the z-axis is given by a distorted plane wave [16,17,20])

$$\Phi_{m_i} = \sum_{S_i l_i} (i)^{l_i} \exp i(\sigma_{l_i} - \sigma_0 + \delta_{l_i}) \sqrt{4\pi(2l_i+1)}\, \frac{u_{l_i}(k_i r)}{k_i r}\, \mathcal{Y}^0_{l_i}(\vartheta, \varphi) \chi^{m_i}_{S_i}, \tag{5}$$

where l_i is the orbital angular momentum of a partial wave, $\sigma_{l_i} - \sigma_0$ is the usual Coulomb phase difference, δ_{l_i} represents the nuclear phase shift †, $\chi^{m_i}_{S_i}$ is the spin function for the channel spin S_i and k_i is the projectile wave number. In the case of a

† It is assumed that there is no resonance in the beam energy range considered so that the δ_{l_i} phase shifts are essentially j-independent (see also subsect. A.1.4 of the appendix).

square-well potential (see subsect. 2.2), the radial wave function $\{u_{l_i}(k_i r)/k_i r\}$ is given analytically by a spherical Bessel function for $r \leqq R_0$ (the nuclear radius) which is matched at R_0 to the exterior Coulomb function $\{F_{l_i}(k_i r)\cos\delta_{l_i} + G_{l_i}(k_i r)\sin\delta_{l_i}\}/k_i r$. The radial wave function is normalized asymptotically to unit flux.

The final-state wave function describing the bound state of the combined system B is written [16, 17, 20]) as

$$\Phi_{m_f} = \sum_{S_f l_f} a_{S_f} \frac{u_{l_f}(k_f r)}{r} \sum_{\beta} (l_f m_f - \beta, S_f \beta | J_f m_f) \mathcal{Y}_{l_f}^{m_f-\beta}(\vartheta, \varphi)\chi_{S_f}^{\beta}, \tag{6}$$

where $u_{l_f}(k_f r)/r$ is again (for a square-well potential) a spherical Bessel function for $r \leqq R_0$ matched to a Whittaker function at R_0 with overall unit normalization so that $\int_0^\infty u_{l_f}^*(k_f r) u_{l_f}(k_f r)\mathrm{d}r = 1$; S_f is the final channel spin and $l_f(J_f)$ is the final orbital (total) angular momentum of the combined system B. The channel spin amplitudes are normalized to $\sum_{S_f}|a_{S_f}|^2 = 1$.

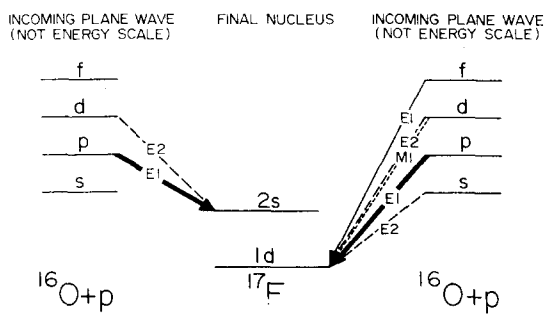

Fig. 1. Schematic transition scheme for the direct-capture process from a plane wave (^{16}O+p) to final 2s and 1d orbits (^{17}F), considering only the lowest multipoles E1, M1 and E2.

If the above wave functions are inserted into the matrix element of eq. (2), the total cross section, in the case of E1 direct capture, is given † by

$$\sigma(\mathrm{E1}) = 0.0716\mu^{\frac{1}{2}}\left(\frac{Z_1}{M_1} - \frac{Z_2}{M_2}\right)^2 \frac{E_\gamma^3}{E_p^{\frac{3}{2}}} \frac{(2J_f+1)(2l_i+1)}{(2j_p+1)(2j_t+1)(2l_f+1)} (l_i 010|l_f 0)^2 R_{l_i l_f}^2 \ \mu\mathrm{b}, \tag{7}$$

where μ is the reduced mass, E_p is the projectile energy (MeV) in the c.m. system and $R_{l_i l_f}$ represents the radial integral (subsect. 2.2). The latter integral has to be evaluated numerically. The Clebsch-Gordan (CG) coefficient $(l_i\, 010|l_f 0)^2$ represents the usual selection rule for E1 transitions. It should be noted that the energy dependence of the cross section depends relatively little on the factor $E_\gamma^3/E_p^{\frac{3}{2}}$ since E_γ varies linearly with E_p, but strongly on the radial integral.

† The total cross section formula for E1 direct capture has been extended recently for deformed nuclei [52]). In this case, the above formula has to be multiplied by $2(C_{j\alpha})^2/(2j+1)$ where j refers to the spin of the final orbit and $C_{j\alpha}$ is the Nilsson expansion coefficient. The index α specifies the Nilsson orbit.

If E1 transitions from two different partial waves (l_i and l_i+2) can proceed to a single-valued final orbit (fig. 1), the E1 contribution from the (l_i+2) partial wave cannot be neglected. The latter contribution can, at higher beam energies, be of the same order of magnitude as the E1 contribution from the lower partial wave (fig. 5). The existence of both contributions is manifested in the energy dependence of the total cross section (fig. 5) as well as in interference effects in the γ-ray angular distributions (subsect. 2.3.1 and appendix A.1.2). The total cross section is, in this case, given by an incoherent sum over l_i (see below). If the final state contains a mixture of various orbital angular momenta l_f, then the total cross section must also be summed over l_f:

$$\sigma(\mathrm{E1}) = \sum_{l_i l_f} \sigma(\mathrm{E1}, l_i \rightarrow l_f). \tag{8}$$

The effective charge factor, $F = (Z_1/M_1 - Z_2/M_2)^2$, in the expression for σ(E1) governs to a large extent the order of magnitude of the direct capture cross section for various projectiles. For proton (or neutron) capture by any target nucleus, $F \approx \frac{1}{4}$. For ^{4}He (or d) capture by any self-conjugate target nucleus, $F \approx 0$. For capture of these projectiles by other target nuclei (except for very light nuclei), the F-factor is always very small compared to that for proton capture. In the example $^{15}\mathrm{N}(\alpha, \gamma)^{19}\mathrm{F}$ where $F \approx \frac{1}{900}$, the E1 cross section is reduced by a factor 220 when compared with proton capture. For ^{3}He capture [e.g. $^{15}\mathrm{N}(^3\mathrm{He}, \gamma)^{18}\mathrm{F}$], the reduction is not as strong ($\approx$ factor 6).

The M1 and E2 contributions to the direct capture process (fig. 1) are usually negligible compared to the E1 contributions. The M1 contribution is reduced, with respect to the E1 contribution, by a factor $(v/c)^2$ which amounts to $< 0.6\%$ at $E_p < 3$ MeV as an order of magnitude estimate. Detailed calculations show that the M1 and E2 contributions amount to less than 0.1% of the dominant E1 contribution. If however the E1 contribution is inhibited, then the M1 and E2 transitions may form the dominant contributions in the direct capture process. Such an inhibition could be due to the F-factor (see above).

2.2. RADIAL INTEGRALS, ENERGY DEPENDENCE OF σ(E1) AND SPECTROSCOPIC FACTORS

The target projectile interaction is assumed to be represented by a simple square-well potential of depth V_0 and radius R_0 in the nuclear interior plus the usual Coulomb potential outside the nucleus. The square-well potential was chosen rather than a Woods-Saxon potential both because of its analytical simplicity and because the direct capture process, which occurs largely outside the nucleus at low beam energies (see below and fig. 4), depends only on the tail of the radial wave function for the bound state. The latter is described by a Whittaker function for both potentials. In order to get approximately the same radial wave function for both potentials one must choose a larger radius R_0 for the square-well potential than the mean radius for a diffuse-edged potential to arrive more nearly at the radius where the nuclear

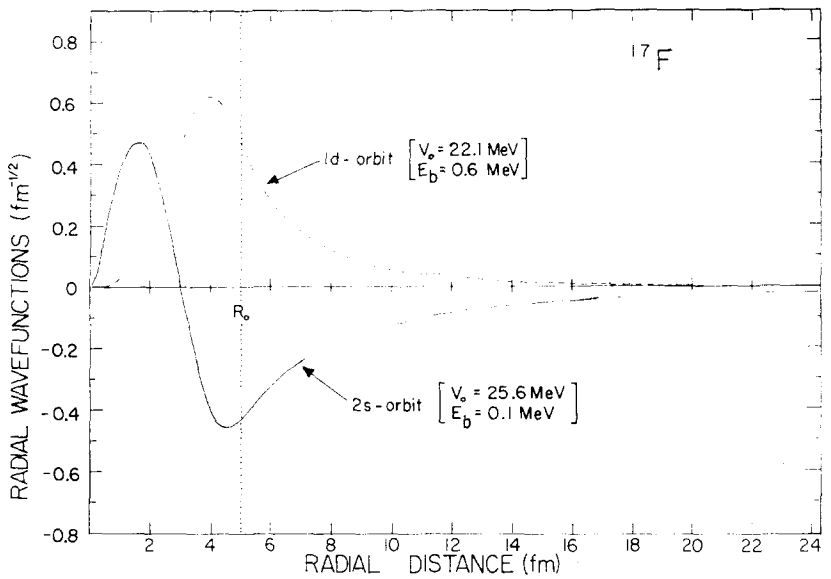

Fig. 2. Normalized radial wave functions of the 1d and 2s single-particle states in ^{17}F for a square-well potential of radius R_0 and well depth V_0. For the indicated nuclear radius $R_0 = 4.8$ fm, the well depth V_0 was adjusted to reproduce the observed binding energies E_b of the two states.

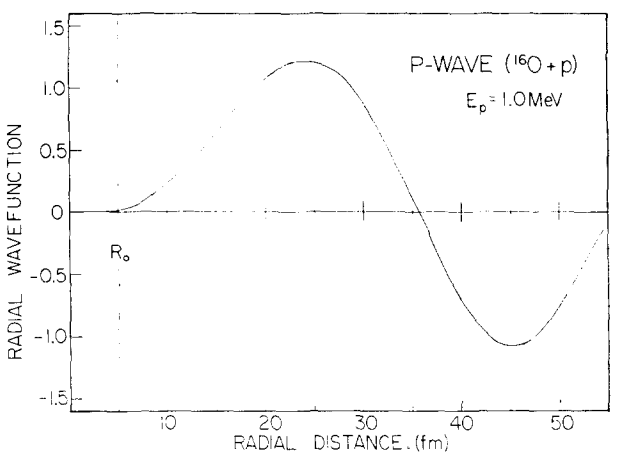

Fig. 3. Radial wave function for partial p-wave ($l_1 = 1$) of the {^{16}O+proton} system at $E_p = 1.0$ MeV. The nuclear phase shift $\delta_{l_1=1}$ has been assumed to be given by the hard-sphere phase shift at $R_0(\delta_1 = -3°)$.

forces have so decreased that the Coulomb forces become dominant. This has been discussed in some detail in refs. [20, 65]). Calculations have shown [20]) that in the case of ^{16}O(p, γ)^{17}F a nuclear radius of $R_0 = 4.8$ fm essentially satisfies the above requirements. In all present calculations it is assumed therefore that the nuclear radius is given by $R_0 = r_0(M_1^{\frac{1}{3}}+M_2^{\frac{1}{3}})$ with $r_0 = 1.36$ fm.

For the bound states, the potential depth V_0 is adjusted to fit the observed binding energy of the state of interest. Fig. 2 illustrates two examples of normalized radial wave functions, namely of the ground-state (1d orbit) and 0.50 MeV first excited state (2s orbit) in ^{17}F. Due to the low binding energies, the radial wave functions for both states extend over wide spatial ranges outside the nuclear radius R_0 with significant amplitudes.

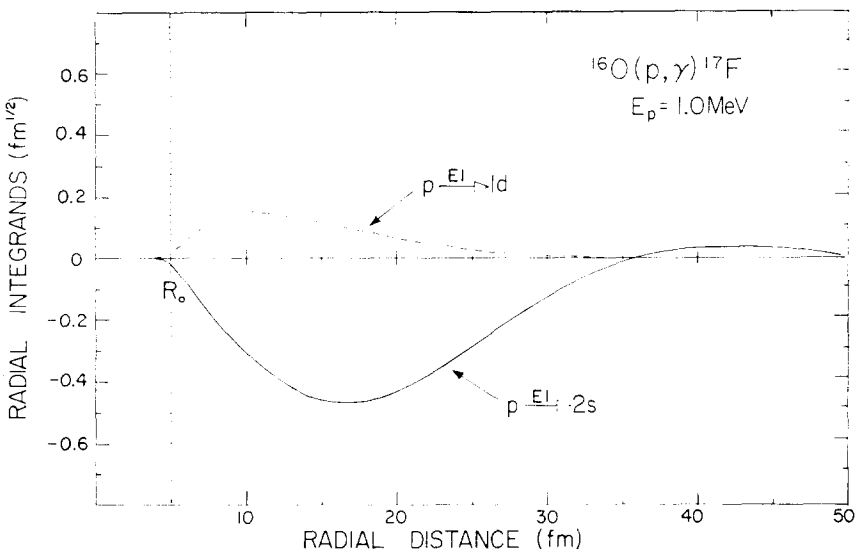

Fig. 4. Radial integrands for direct radiative proton capture from a p-wave to 1d and 2s single-particle states in ^{17}F at $E_p = 1.0$ MeV. The major contributions in the integrands arise, in both cases, from regions far outside the nuclear radius R_0.

The calculation of the radial wave functions for the continuum states require a knowledge of the nuclear phase shifts δ_l. In principle, these phase shifts can be obtained from a phase shift analysis of elastic scattering data. In the case of ^{16}O(p, p)^{16}O, the analysis of the available scattering data at $E_p < 2.5$ MeV reveals [45]) that all these phase shifts $\delta_l (l = 0$ to 3) are too small ($< 8°$) to be extracted from the data with any degree of accuracy. They were assumed therefore to be given by the hard-sphere phase shifts ($\approx 1°$–$9°$) at the nuclear radius R_0. Fig. 3 illustrates an example of a radial wave function for a partial p-wave at $E_p = 1.0$ MeV. The wave function is small over the nuclear interior so that the major part of its contribution to the direct capture process should come from the extra-nuclear region.

With the knowledge of the continuum (u_c) and bound (u_b) radial wave functions, the radial integrals

$$R_{l_i l_f} = \int_0^\infty u_c(r) \mathcal{O}_{E1}(r) u_b(r) r^2 \mathrm{d}r \tag{9}$$

are evaluated numerically. The radial integrands for the E1(p → 2s) and E1(p → 1d) transitions in $^{16}O(p, \gamma)^{17}F$ are shown in fig. 4. The results demonstrate that the major part of the process is dominated by contributions from regions far outside the nuclear radius R_0.

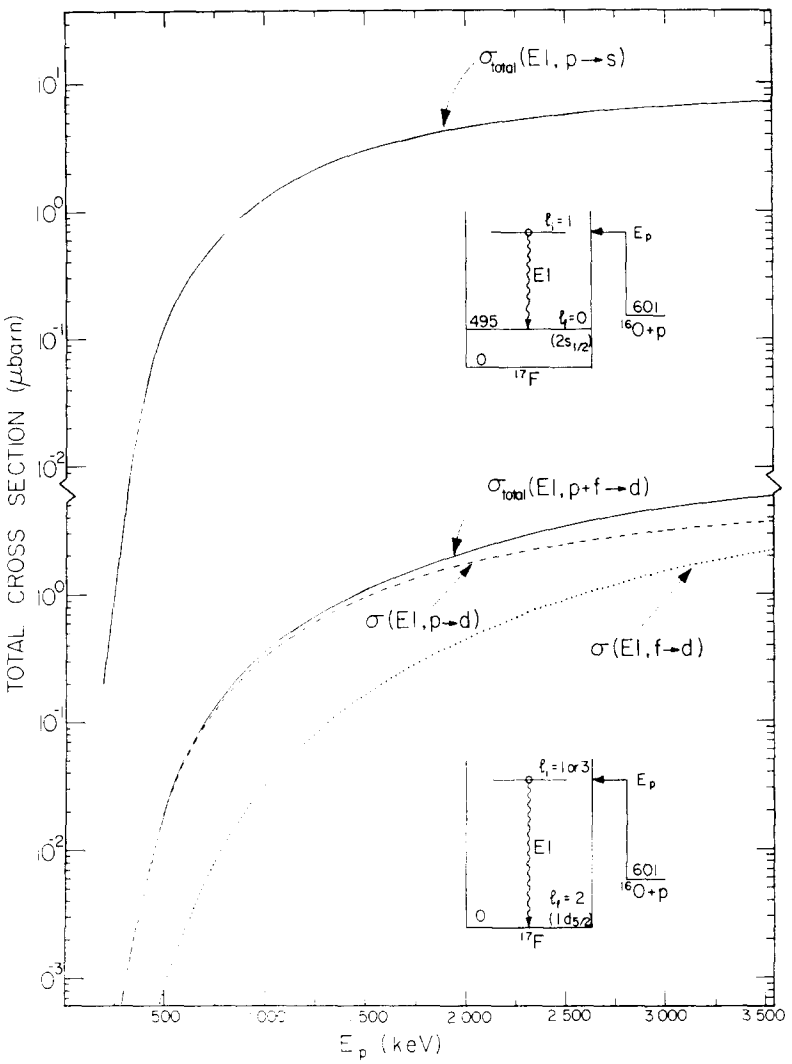

Fig. 5. Theoretical total cross sections as a function of beam energy for the $^{16}O(p,\gamma)^{17}F$ reaction deduced from the direct-capture model.

The energy dependence of $\sigma(E1)$ is mainly ruled, in the low-energy region, by transmission through the Coulomb and centrifugal barriers, whereas at the higher energies the energy dependence follows principally the factor $E_\gamma^3/E_p^{\frac{1}{2}}$. Theoretical examples of such $\sigma(E1)$ curves are presented in fig. 5 for E1 transitions to the $1d_{\frac{5}{2}}$ and

$2s_{\frac{1}{2}}$ orbits at 0 and 0.50 MeV in ^{17}F, respectively. The Coulomb barrier for ^{16}O+p is at $\approx$ 2.4 MeV. It should be noted that due to the higher centrifugal barrier the σ(E1, f $\rightarrow$ d) cross section has a different energy dependence than σ(E1, p$\rightarrow$ d).

From the comparison of the experimental and theoretical absolute cross sections, nuclear structure information in the form of spectroscopic factors for the final states can be obtained (see below). Like all nuclear quantities which involve radial matrix elements, the spectroscopic factor depends on the assumed nuclear radius R_0. A calculation showed that a change of 10% in R_0 corresponds roughly to a change of 15% in the theoretical cross section and hence in the deduced spectroscopic factor.

The spectroscopic factors, $C^2S(l_f)$, are extracted from the data using the usual relation

$$\sigma_{exp} = \sum_{l_f} C^2S(l_f)\sigma_{theo}(l_f), \tag{10}$$

where $\sigma_{theo}(l_f)$ is the theoretical cross section. The isospin Clebsch-Gordan coefficient C^2 is given by $(t_p m_p t_t m_t | T_f M_f)^2$ where t_p, t_t and T_f represent the isospins of the projectile, target nucleus and final state, respectively.

2.3. EXPRESSIONS FOR γ-RAY ANGULAR DISTRIBUTIONS

In the following subsections, general expressions for the γ-ray angular distributions of direct capture (primary) and subsequent nuclear decay (secondary) transitions will be discussed. Illustrative examples, relevant to the subsequent experiments, will also be presented. The derivation of these expressions is described in the appendices.

2.3.1. Direct capture transitions. The angular distribution for the direct capture γ-ray transition is given (appendix A.1.1) by:

$$W(\vartheta) = \sum_k (l_i 0 l_i 0 | k0) Z_1(L l_i L l_i; l_f k) Q_k P_k(\vartheta). \tag{11}$$

These expressions depend only on the orbital angular momenta l_i and l_f of the initial and final state, respectively and on the multipole order, L, of the γ-ray transition. They are independent of the total spin J of the final state as well as of the intrinsic spins of the target nucleus j_t and projectile j_p (i.e. the channel spin $\boldsymbol{S} = \boldsymbol{j}_p + \boldsymbol{j}_t$). Examples of the most common angular distributions observed in the present work are:

$$\begin{aligned}
&\text{E1(p} \rightarrow \text{s)} \qquad W(\vartheta) = 1 - P_2(\vartheta) = \sin^2 \vartheta, \\
&\text{E1(p} \rightarrow \text{d)} \qquad W(\vartheta) = 1 - \tfrac{1}{10} P_2(\vartheta) = 1 + \tfrac{1}{6} \sin^2 \vartheta, \\
&\text{E1(f} \rightarrow \text{d)} \qquad W(\vartheta) = 1 - \tfrac{2}{5} P_2(\vartheta) = 1 + \sin^2 \vartheta.
\end{aligned}$$

A sensitive test of the above theoretical angular distributions is provided by the study of the direct capture process in the two reactions ^{16}O(p, γ)^{17}F and ^{17}O(p, γ)^{18}F. The angular distributions to final states with the same orbit l_f should be identical in the two reactions despite the different target spins (j_t = 0 and $\frac{5}{2}$) as well as the different possible total spins ($\boldsymbol{J}_f = \boldsymbol{S} + \boldsymbol{l}_f$). Examples are described in subsects. 4.1 and 4.2.3.

In previous studies of the direct capture process of protons by light nuclei, including $^{16}O(p,\gamma)^{17}F$, $El(p \rightarrow s)$ direct capture transitions have been identified on the basis of observed large anisotropies alleged to be of the type $W(\vartheta) = \sin^2\vartheta$. However, in most of these examples, where targets with spin $j_t = 0$ or $\frac{1}{2}$ were used, the large observed anisotropies could also have been due to the tails of distant resonances †. The situation is different for $^{17}O(p,\gamma)^{18}F$ where due to the poor alignment in the reaction ($|m| \leqq 3$), the γ-ray angular distributions from resonant states with spins $J \leqq 3$ are isotropic or nearly isotropic [refs. [32-35]) and figs. 13–15]. For γ-ray transitions to final states in ^{18}F with $l_f = 0$ (i.e. $J^\pi = 2^+$ or 3^+ states), the observation of large anisotropies of the type $W(\vartheta) = \sin^2\vartheta$ would now clearly demonstrate the presence of the direct capture process.

For E1 transitions, which proceed from two initial partial waves l_i and $l_i^* = l_i + 2$ (subsect. 2.1 and fig. 1), the γ-ray angular distribution includes an interference term $W^{int}_{l_i, l_i*}(\vartheta)$ [appendix A.1.2] between the two E1 transitions:

$$W(\vartheta) = \frac{1}{1+y}\left[W_{l_i}(\vartheta) + yW_{l_i*}(\vartheta) + 2\sqrt{y}\cos\varepsilon W^{int}_{l_i l_i*}(\vartheta)\right], \tag{12}$$

where y represents the ratio of the cross sections, $y = \sigma(l_i^* \rightarrow l_f)/\sigma(l_i \rightarrow l_f)$, and ε is a phase factor given by the usual Coulomb (φ_{l_i}) and nuclear phase shifts (δ_{l_i}): $\varepsilon = \varphi_{l_i*} - \varphi_{l_i} + \delta_{l_i*} - \delta_{l_i}$. The ratio y can be obtained from the direct capture model calculations (e.g. fig. 5), the φ_{li} from the usual expressions for the Coulomb phases [26,27]) and the δ_{l_i} from a phase shift analysis of elastic scattering data. For the example $El(p \rightarrow d)$ and $El(f \rightarrow d)$, the interference term is

$$W^{int}_{pf}(\vartheta) = \tfrac{3}{5}\sqrt{\tfrac{3}{2}}P_2(\vartheta),$$

and hence

$$W(\vartheta) = 1 + \frac{-0.10 + 1.47\sqrt{y}\cos\varepsilon - 0.40y}{1+y}P_2(\vartheta).$$

For the particular case of direct capture at $E_p = 1.10$ MeV in $^{16}O(p,\gamma)^{17}F$ to the $d_{\frac{5}{2}}$ ground state, the above angular distribution formula becomes

$$W(\vartheta) = 1 + 0.13\,P_2(\vartheta),$$

where $y = 0.10$ (fig. 5) and $\varepsilon \approx 53°$ ($\Delta\varphi = 53°$, $\Delta\delta \leqq 5°$). Even though the $El(f \rightarrow d)$ transition amounts to only 10% of the total cross section at $E_p = 1.10$ MeV, its contribution is amplified through the large interference term ($\sqrt{y} \approx 30\%$). The effect of the interference is to change the sign of the a_2 coefficient. Since all parameters are determined by the direct capture model, a measurement of the angular distribution of the above type at several beam energies represents a further important and sensitive test on the validity of the model (subsect. 4.1 and fig. 8).

† An angular distribution of a pure type $W(\vartheta) = \sin^2\vartheta$ cannot be obtained, however, easily from a single resonance state.

If the final state is described by two orbital angular momenta, l_f and $l_f^* = l_f+2$, the γ-ray angular distribution can be expressed, within the framework of this model, as an incoherent sum of the individual γ-ray angular distributions (appendix A.1.2) weighted by the ratio of the cross sections $z = \sigma(l_i \to l_f^*)/\sigma(l_i \to l_f)$:

$$W(\vartheta) = \frac{1}{1+z}[W(\vartheta, l_i \to l_f) + zW(\vartheta, l_i \to l_f^*)]. \tag{13}$$

The ratio z can be extracted from the experimental data and is obviously an important value to obtain since it reveals information on the two components l_f and l_f^* in the final-state wave functions. For the more complicated case of orbital mixing in the initial as well as final state, no further parameters than z are required in the analysis, since the orbital mixing in the initial state is determined entirely by the model (see above). Examples will be discussed in subsect. 4.2.3.

2.3.2. Secondary transitions. The γ-ray angular distribution for subsequent secondary γ-radiation following the direct capture transition is given (appendix A.2) by:

$$W(\vartheta) = \sum_{kL_2L_2^*} (l_i 0 l_i 0|k0) W(l_i l_f l_i l_f; L_1 k) \times W(J_f l_f J_f l_f; Sk)\delta^r \bar{Z}_1(L_2 J_f L_2^* J_f; J_e k) Q_k P_k(\vartheta), \tag{14}$$

where L_1 and (L_2, L_2^*) are the multipoles of the primary and secondary γ-ray transitions, respectively, δ^r represents the multipole mixing ratio of the secondary transition [26]), S is the channel spin ($\boldsymbol{S} = \boldsymbol{j}_t + \boldsymbol{j}_p$) and J_f and J_e are the total spins of the states involved in the secondary transition ($J_f \to J_e$). The first Racah coefficient $W(l_i l_f l_i l_f; L_1 k)$ corresponds as usual [26, 27]) to the "unobserved" primary transition and the second Racah coefficient represents the transformation from the orbital angular momenta representation to the total spin representation. Due to the complexity of the above expression, no examples will be given here. The use of the formula in the experimental analysis of the secondary γ-ray angular distributions is described in subsect. 4.2.4.

An interesting feature of the direct capture process for target spins $j_t \neq 0$ concerns the angular distribution of the secondary transitions where $l_f = 0$. In this case the direct capture primary has a large anisotropy of the type $W(\vartheta) = \sin^2\vartheta$ and the secondary transition is isotropic (independent of J_f). In the analogous nuclear case of a γ-γ cascade, large positive anisotropies in the primary transition usually imply also anisotropies in the secondary transition for intermediate states with $J_f \geqq 1$. This difference is due to the fact that the direct capture process itself selects only the $l_f = 0$ component in the total wave function of the J_f state, which is not the case for a nuclear γ-ray decay.

For a mixture of orbital angular momenta, l_f and l_f+2, in the final-state wave function, the angular distribution of the secondary transitions is given by the incoherent sum of the two components from eq. (14) weighted by the ratio z (see eq. (13)). This represents, therefore, a useful consistency check on the information deduced from the primary transition.

Furthermore, information of the j_f value of the final orbit ($j_f = l_f - \frac{1}{2}$ and/or $j_f = l_f + \frac{1}{2}$ for direct proton capture) can be deduced from the secondary γ-ray angular distributions. This is of special interest for the case of direct capture by target nuclei with $j_t \neq 0$. If S_1 and S_2 are the two possible channel spins with $W_{S_i}(\vartheta)$ given by eq. (14), the observed angular distribution is described by

$$W(\vartheta) = \frac{1}{1+t}[W_{S_1}(\vartheta) + tW_{S_2}(\vartheta)]. \tag{15}$$

The channel spin intensity ratio t is defined by $t = I(S_2)/I(S_1)$ and can be deduced from the experiment. This value of t can then be compared with descriptions based on the L-S or j-j coupling schemes [46]). In the j-j coupling scheme, $I(S)$ is given by

$$I(S) = \sum_{j_f j_f^*} \sqrt{(2j_f+1)(2j_f^*+1)}(2S+1)W(l_f\, j_p J_f\, j_t;\, j_f S)W(l_f\, j_p J_f\, j_t;\, j_f^* S)x^r(2-\delta_{r1}), \tag{16}$$

where x represents the amplitude ratio $x = A(j_f^*)/A(j_f)$. The exponent r has the value 0, 1 or 2 depending on whether the term is of the type $j_f j_f$, $j_f j_f^*$, or $j_f^* j_f^*$, respectively, and δ_{r1} represents the Kronecker symbol. Examples are described in subsect. 4.2.4.

2.4. HIGHER ORDER EXCITATION EFFECTS

The direct capture mechanism, as described above, represents a single-step process where the incident projectile radiates a photon and enters a shell-model orbit of the target nucleus. The target nucleus acts mainly as a spectator in this process.

In heavier nuclei ($A > 40$) it has been observed [49-52]) that this direct capture model fails by an order of magnitude to fit the observed capture cross sections for incident nucleon energies of 10 to 20 MeV. This discrepancy has been satisfactorily removed by the inclusion of a "semi-direct" (or "collective") capture mechanism [49, 50]) in addition to the direct capture mechanism. This semi-direct process is described [49, 50]) by a nuclear interaction between the incident projectile and the target nucleus. This interaction leads to an intermediate state with the particle in a bound state and the target nucleus excited in its giant dipole resonance, which then decays by the emission of γ-rays. Due to the collective mode of the giant dipole oscillations, the cross section for this two-step process predominates over that of the direct capture process in the region of the giant dipole resonance for the nuclei mentioned above [49-52]).

In view of the significance of the spectroscopic factors deduced from the experimental direct capture cross sections (subsect. 2.2), it is important to know the contribution of this semi-direct process to the observed cross sections. In light nuclei, giant dipole resonances are observed [47]) at excitation energies of $E_x \approx 20$–25 MeV with a width $\Gamma \approx 3$–5 MeV. For this assumption, the contribution of the semi-direct process is $< 0.1\%$ at low beam energies ($E_p < 3$ MeV) and is therefore negligible.

An additional two-step process of interest is that of direct capture from an excited target state. An order of magnitude estimate of the size of this effect can be obtained by assuming that the process can be described first by the Coulomb excitation of the target nucleus to an excited state, and then by subsequent direct capture of the projectile. Since the two processes have similar small cross sections ($\approx$ 1–50 μb), no significant contribution from this two-step process is expected. If a theoretical treatment similar to that for the semi-direct process [49, 50]) is used, the cross section is proportional to $B_{i\to f}(EL)/E_f^2$ where Coulomb excitation has been restricted solely to the first excited state. For $^{17}O(p,\gamma)^{18}F$ where $E_f = 0.87$ MeV, one has $B_{2\to 1}(E2) = 2\times 10^{-4}\ e^2\cdot b$ [ref. [38])], and for $E_p < 2$ MeV the two-step process contributes only 0.003% to the total cross section. A more favourable case in the search for this two-step process would be the reaction $^{19}F(p,\gamma)^{20}Ne$ due to the large $B(E2)$ value for the $0(\frac{1}{2}^+) \to 0.20(\frac{5}{2}^+)$ MeV transition [59]) and the low excitation energy of the first excited state in ^{19}F. At $E_p = 1.5$ MeV, the two-step process should contribute a few percent ($\approx$ 3%) to the total cross section. However the small contribution is increased to a larger effect ($\approx$ 14%) by the interference term between the single and two-step processes and should be observable. Furthermore, the formation of the $J^\pi = 4^+$ state at 4.25 MeV in ^{20}Ne is forbidden in the single-step process if the l_f value of the captured particle is restricted to the (2s, 1d) shell. Thus, if this state has parentage in the $197(\frac{5}{2}^+)$ keV state in ^{19}F (i.e. $\frac{5}{2}^+ \otimes d_{\frac{5}{2}(\frac{3}{2})}$), the two-step process will provide the only contribution to its formation.

3. Experimental equipment, procedure and analysis

The low cross sections for the direct radiative capture reactions and the low efficiency of high-resolution Ge(Li) detectors require the use of ion beam currents as high as possible in order to improve the signal-to-noise ratio. In the present work, proton beams of 120 μA were supplied by the 1 MV JN Van de Graaff accelerator at the University of Toronto and proton beams of 150 to 200 μA by the 3 MV KN Van de Graaff accelerator at McMaster University, Hamilton. The beam was focussed into a profile 3 mm wide and 20 mm high.

The high power input into the target backing (several hundred Watts) makes direct cooling of the target backing necessary. Details concerning target chamber design, charge measurements, suppression of carbon accumulation on the targets, preparation and choice of targets and target backings have been recently described [30, 31]). Due to the low direct-capture γ-ray yield, special care in target preparation has to be taken in order to avoid the usual troublesome contaminant reactions (p, $\alpha\gamma$) on e.g. ^{15}N, ^{19}F or ^{23}Na contaminants. The ^{16}O targets were produced by anodizing 0.25 mm thick Ta sheets in distilled water as well as in water depleted in ^{18}O (^{17}O) with isotopic residue of 0.0045 (0.002)%. The ^{17}O targets have been fabricated in a way similar to that reported previously [31]). All targets were able to withstand

bombardment with beam currents of 200 μA for periods greater than 5 d without noticeable deterioration.

The good energy resolution of Ge(Li) detectors facilitates the measurement of such low γ-ray cross sections due to an improved signal-to-noise ratio, when compared with NaI(Tl) detectors. In the present work, the γ-rays have been therefore observed with 45 and 50 cm^3 Ge(Li) detectors. The energy resolution of these detectors was typically 2.0 keV at $E_\gamma = 1.3$ MeV.

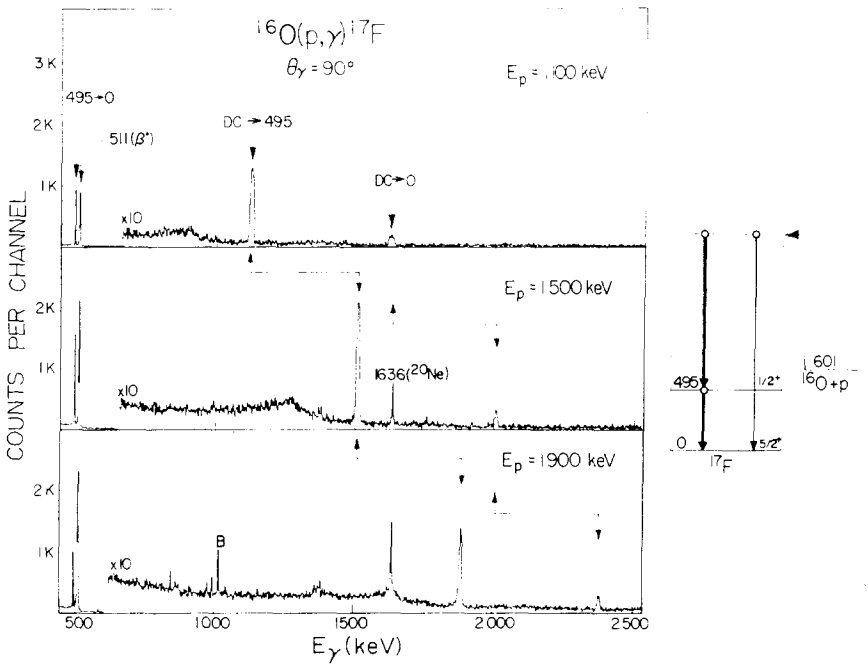

Fig. 6. Sample γ-ray spectra of the $^{16}O(p,\gamma)^{17}F$ reaction obtained with the 45 cm^3 Ge(Li) detector at a distance of $D = 8$ cm from the target. An anodized $Ta_2{}^{16}O_5$ target (depleted in ^{17}O and ^{18}O) was used.

Direct-capture γ-ray transitions are identified practically on the basis of the following criteria:

(i) the energies E_γ of the direct-capture γ-rays vary with the projectile energy E_p in a way given by the kinematics of the reaction (fig. 6);

(ii) the observed peak width of the direct-capture transitions to bound states is dependent on the target thickness due to the smooth cross section of the reaction (figs. 6 and 10);

(iii) the observation of γ-ray angular distributions of the form $W(\vartheta) = \sin^2\vartheta$ represents a clear signature for the presence of the direct capture process (figs. 7, 8 and 15);

(iv) the energy dependence of the differential cross sections for the individual γ-ray

transitions must follow the predictions of the direct-capture model (see also below).

Furthermore, the identification of direct-capture transitions to excited states can be verified by the observation of the known γ-decay schemes of the final states.

In the present work, targets of 8–10 keV thickness at $E_p = 1.5$ MeV were used which facilitate the identification of primary transitions (criterion (ii) above) in a complex γ-ray spectrum like the one shown in fig. 10 (cross-hatched peaks).

A few comments are in order here on the analysis and interpretation of γ-ray angular distributions and yield curves. For radiative capture of protons on doubly even target nuclei to $J^\pi = \frac{1}{2}^+$ final states (i.e. $l_f = 0$ orbit), the predicted angular distributions for the γ-ray transitions to these states are of the form $W(\vartheta) = \sin^2\vartheta$ at all beam energies due to E1(p → s). This has been observed in the reaction ^{16}O(p, γ)^{17}F to the 0.50 ($\frac{1}{2}^+$) MeV state (fig. 8) and in the reaction ^{18}O(p, γ)^{19}F to five $J^\pi = \frac{1}{2}^+$ final states [57]). However for the reaction ^{24}Mg(p, γ)^{25}Al, the angular distribution for the direct-capture transition to the 0.45($\frac{1}{2}^+$) MeV state in ^{25}Al was described [56]) by $W(\vartheta, E_p) = a(E_p) + b(E_p) \sin^2\vartheta$. This deviation can be accounted for as the consequence of interference with resonances in the reaction [56]). For the reaction ^{17}O(p, γ)^{18}F, direct capture to final states with $J^\pi = 2^+$ or 3^+ can be characterized by $l_f = 0$ and $l_f = 2$ orbits with $W(\vartheta) = \sin^2\vartheta$ and $W(\vartheta) = \alpha + \beta \sin^2\vartheta$ with $\alpha > \beta$, respectively (subsect. 2.3.1). For a mixture of both $l_f = 0$ and $l_f = 2$ in the final state, the angular distribution is $W(\vartheta, E_p) = a(E_p) + b(E_p) \sin^2\vartheta$. A significant yield at $\vartheta = 0°$ reveals immediately the presence of an $l_f = 2$ component in the final-state wave function. However the latter interpretation is not unique since distant broad resonances can contribute to the yield at 0° (cf. ^{24}Mg(p, γ)^{25}Al quoted above). For these reasons, the differential cross sections for all direct capture γ-rays have been measured, concurrently at $\vartheta = 0°$ and 90°, over a wide range of beam energies (figs. 11 and 13–15).

4. Results and conclusions

4.1. THE ^{16}O(p, γ)^{17}F REACTION

Due to the tightly bound ^{16}O core, the two observed bound states at $E_x(J^\pi) = 0(\frac{5}{2}^+)$ and 0.50($\frac{1}{2}^+$) MeV in ^{17}F should be well described by a single-particle model. The ^{16}O(p, γ)^{17}F reaction then provides a good means for testing the validity of the direct capture model. There is no resonant state formed [38]) below $E_p = 2.5$ MeV so that the direct-capture process can be studied over a wide range of beam energies without complications of interfering resonances. Excitation functions and total cross sections for this reaction determined from the measurement of the β^+ activity of ^{17}F have been previously [5, 6]) reported. Detailed studies of the direct-capture γ-ray transitions have been only reported for limited beam energy ranges [4, 7]).

Sample γ-ray spectra are shown in fig. 6. The excitation functions of the direct capture transitions, measured concurrently at 0° and 90°, are shown in fig. 7. The differential cross sections have been normalized to the cross section of

$\sigma_{tot} = 0.29 \pm 0.03$ μb at $E_p = 616$ keV reported by Tanner [6]). This value is in good agreement with recent absolute cross section measurements [53]). Despite the prominent feature near $E_p = 2.66$ MeV for the DC → 0.50 MeV transition (see below), the yields of both direct-capture transitions increase smoothly with beam energy.

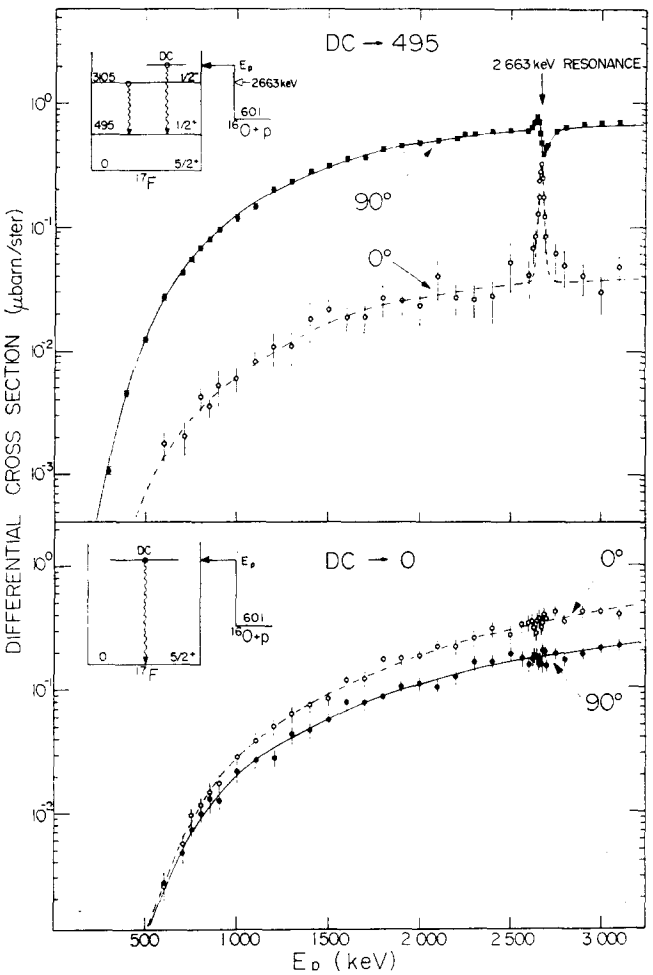

Fig. 7. The differential cross sections for the direct-capture γ-ray transitions to the 0.50 MeV state and to the ground state in ^{17}F, as observed in the ^{16}O(p,γ)^{17}F reaction, are shown as a function of beam energy at two angles of observation. The relative errors are as indicated but are subject to the additional 10% error of the absolute cross section used as the standard (subsect. 4.1). The solid and dashed lines through the data points represent the theoretical predictions.

The smooth yield for the DC → 0.50 MeV γ-ray transition is associated with a $W(\vartheta) = \sin^2\vartheta$ angular distribution as shown in fig. 8 and is also evident from a comparison of the γ-ray yield curves at 0° and 90°. The finite intensities at 0° in fig. 7 are due to the finite solid angle of the γ-ray detector ($Q_2 = 0.94$). The energy

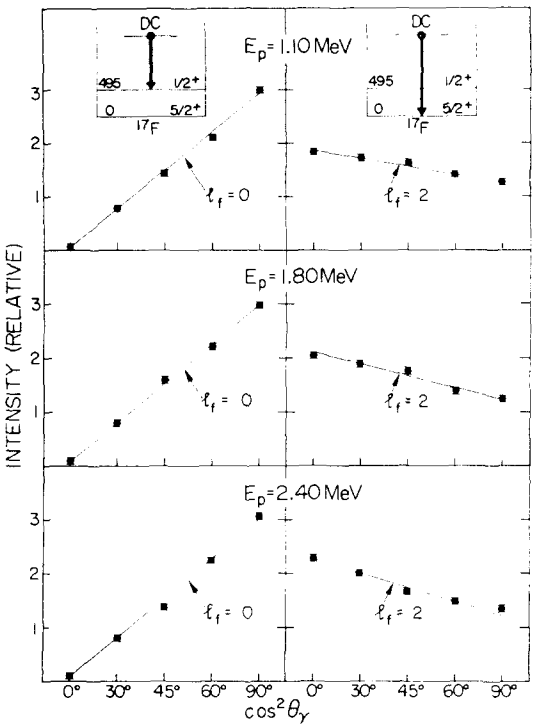

Fig. 8. Angular distributions for the DC → 0 and DC → 0.50 MeV γ-ray transitions as observed in the reaction ^{16}O(p,γ)^{17}F at E_p = 1.10, 1.80 and 2.40 MeV. The solid lines represent model predictions (see text).

TABLE 1

Comparison of absolute spectroscopic factors for states in ^{17}F as obtained from direct capture and stripping reactions

Reaction	Spectroscopic factor $C^2S(l)$	
	Ground state $l = 2$	0.50 MeV state $l = 0$
Present work, ^{16}O(p,γ)^{17}F	0.90	1.00
Stripping, ^{16}O(d, n)^{17}F		
E_d = 8.0 MeV [a])	0.84	0.93
E_d = 9.3 MeV [a])	0.77	0.96
E_d = 7.7 MeV [b])	1.05 } 0.88	1.15 } 0.99
E_d = 11.0 MeV [b])	0.90	0.95
E_d = 12.0 MeV [b])	0.85	0.95

[a]) Ref. [28]).
[b]) Ref. [29]).

dependence of the observed yield and the predictions of the theory (solid and dashed lines in fig. 7) are in good agreement. The angular distributions and yield curves of the differential cross sections reveal a direct capture transition of the type E1(p → s) to the $0.50(\frac{1}{2}^+)$ MeV state. The spectroscopic factor is $C^2S(l_f = 0) = 1.00 \pm 0.14$, in excellent agreement with stripping information (table 1).

The 0° and 90° yield curves for the DC → 0 transition are in good agreement with the model predictions for an E1(p and f → d) transition (fig. 7). The angular distributions for this transition as obtained at $E_p = 1.10$, 1.80 and 2.40 MeV are described by a_2 coefficients of $+0.15 \pm 0.02$, $+0.29 \pm 0.03$ and $+0.37 \pm 0.04$, respectively. These coefficients are consistent with the corresponding theoretical values of $a_2 = +0.13$, $+0.28$ and $+0.34$ (subsect. 2.3.1). From the absolute cross section for this transition, the spectroscopic factor for the ground state in ^{17}F is $C^2S(l_f = 2) = 0.90 \pm 0.15$ again in good agreement with stripping data (table 1).

From the yields of the DC → 0 and DC → 0.50 MeV γ-ray transition observed at 90° and $E_p = 2.56$–2.76 MeV, Domingo [7]) reports single-particle reduced widths for the ground state and 0.50 MeV state of $\vartheta^2(\frac{5}{2}^+) = 0.38 \pm 0.08$ and $\vartheta^2(\frac{1}{2}^+) = 0.57 \pm 0.10$, respectively, where the definition of Lane [62]) has been used for ϑ^2. These reduced widths correspond to spectroscopic factors of $C^2S(\frac{5}{2}^+) = 0.77 \pm 0.16$ and $C^2S(\frac{1}{2}^+) = 1.3 \pm 0.2$ in good agreement with the results from the present work.

The pronounced feature in the DC → 0.50 MeV yield curve at $E_p \approx 2.66$ MeV can be associated with the $3.11(\frac{1}{2}^-)$ MeV resonance state in ^{17}F. This state has been observed [38]) previously as a p-wave resonance, with total width $\Gamma = 19 \pm 1$ keV, in elastic proton scattering on ^{16}O at $E_p = 2663$ keV. The DC → 0 and DC → 0.50 MeV γ-ray yield curves have been studied by Domingo [7]) in the vicinity of this resonance at an angle of $\vartheta_\gamma = 90°$, and an interference pattern only in the DC → 0.50 MeV transition has been observed which is confirmed by the present work (fig. 7). A γ-width of $\Gamma_\gamma \leqq 30$ meV for the expected † 3.11 → 0.50 MeV resonant transition has been deduced [7]). This resonant transition is clearly observed in the present work as a normal resonance peak in the 0° yield curve. The observation of the resonance is favoured at this angle due to the zero yield of the competing direct-capture transition. The pattern at 90° can be explained as an interference between the Breit-Wigner amplitude for the 2663 keV resonance and the direct-capture amplitude (appendix A.3). The known total width of the resonant state and the observed cross sections for the resonant transition at both angles lead to $\Gamma_\gamma = 12 \pm 2$ meV consistent with the upper limit quoted above. The strength of this transition is $M^2(\text{E1}) = (1.5 \pm 0.3) \times 10^{-3}$ W.u. compared with the strength of the analogue transition in ^{17}O of $M^2(\text{E1}) = (1.2 \pm 0.7) \times 10^{-3}$ W.u. If the $3.11(^{17}\text{F})$ and $3.06(^{17}\text{O})$ MeV states are good analogue states, then the two E1 strengths should be identical [64]) which is confirmed within the admittedly large experimental errors.

† The analogue state in ^{17}O at 3.06 MeV is known [38]) to decay 100% to the $0.87(\frac{1}{2}^+)$ MeV state with $\Gamma_\gamma = 5.5 \pm 3.0$ meV.

4.2. THE $^{17}O(p,\gamma)^{18}F$ REACTION

4.2.1. Aims and experimental procedure. As a first approximation, the nucleus ^{18}F may be pictured as a simple system formed by the addition of a proton and a neutron to an inert ^{16}O core. In the *j-j* coupling shell model, the lowest levels available for the added valence nucleons are the $1d_{\frac{5}{2}}$, $2s_{\frac{1}{2}}$ and $1d_{\frac{3}{2}}$ orbitals leading to (2p-0h) states of (2s, 1d) configurations. Shell-model calculations e.g. of the Kuo and Brown type [32]) (KB) predict fifteen positive parity states of such (2p-0h) structure below

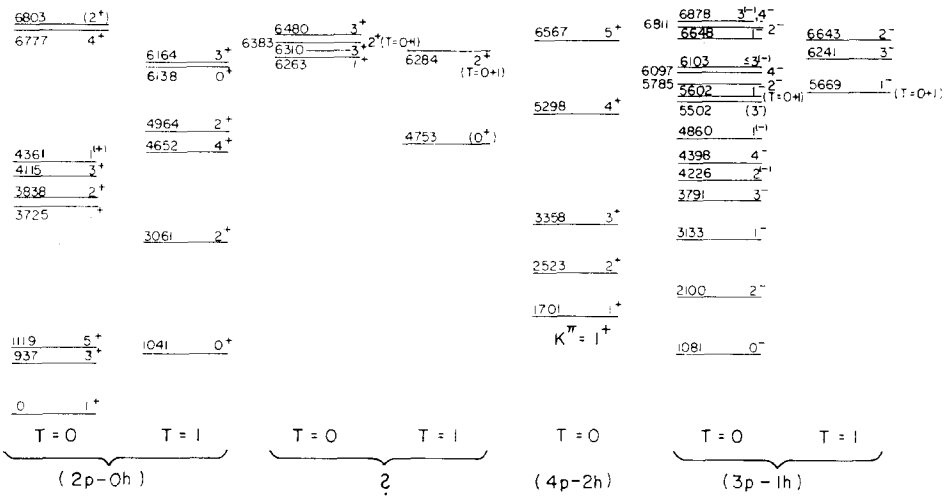

Fig. 9. States in ^{18}F below $E_x = 7$ MeV put into perspective by grouping the states according to common overall structure. The results have been taken from refs. [31–37]).

$E_x = 7$ MeV in ^{18}F. In recent work [32, 35]), fourteen of these model states with (2s, 1d) configurations have been identified with observed states below $E_x = 7$ MeV. In addition, the first five members of an $K^\pi = 1^+$ rotational band of a predominantly (4p-2h) nature have been found [33]). It has been noted that these two groups of states coexist with relatively little interaction between them. Finally, eighteen states of negative parity have been observed and suggested to be predominantly of a (3p-1h) nature [34]). Fig. 9 summarizes these results.

With regard to possible direct capture in the $^{17}O(p,\gamma)^{18}F$ reaction, it is expected that the process proceeds predominantly to states in ^{18}F with configurations of the type $\{|^{17}O(\text{g.s.})\rangle \otimes |\text{ added proton}\rangle\}$. Since the $J^\pi = \frac{5}{2}^+$ ground state in ^{17}O is to a large extent described by a $1d_{\frac{5}{2}}$ single-particle orbit coupled to an inert ^{16}O core (subsect. 4.1), the positive-parity (2p-0h) states which are populated in the direct capture process will be those with $(d_{\frac{5}{2}}, s_{\frac{1}{2}})$, $(d_{\frac{5}{2}}, d_{\frac{3}{2}})$ or $(d_{\frac{5}{2}}, d_{\frac{5}{2}})$ configurations (fig. 9). The exceptions within this group are the $3.73(1^+)$ and $6.14(0^+, T = 1)$ MeV states which have been identified [32]) with the model states of predominantly $(s_{\frac{1}{2}})^2$

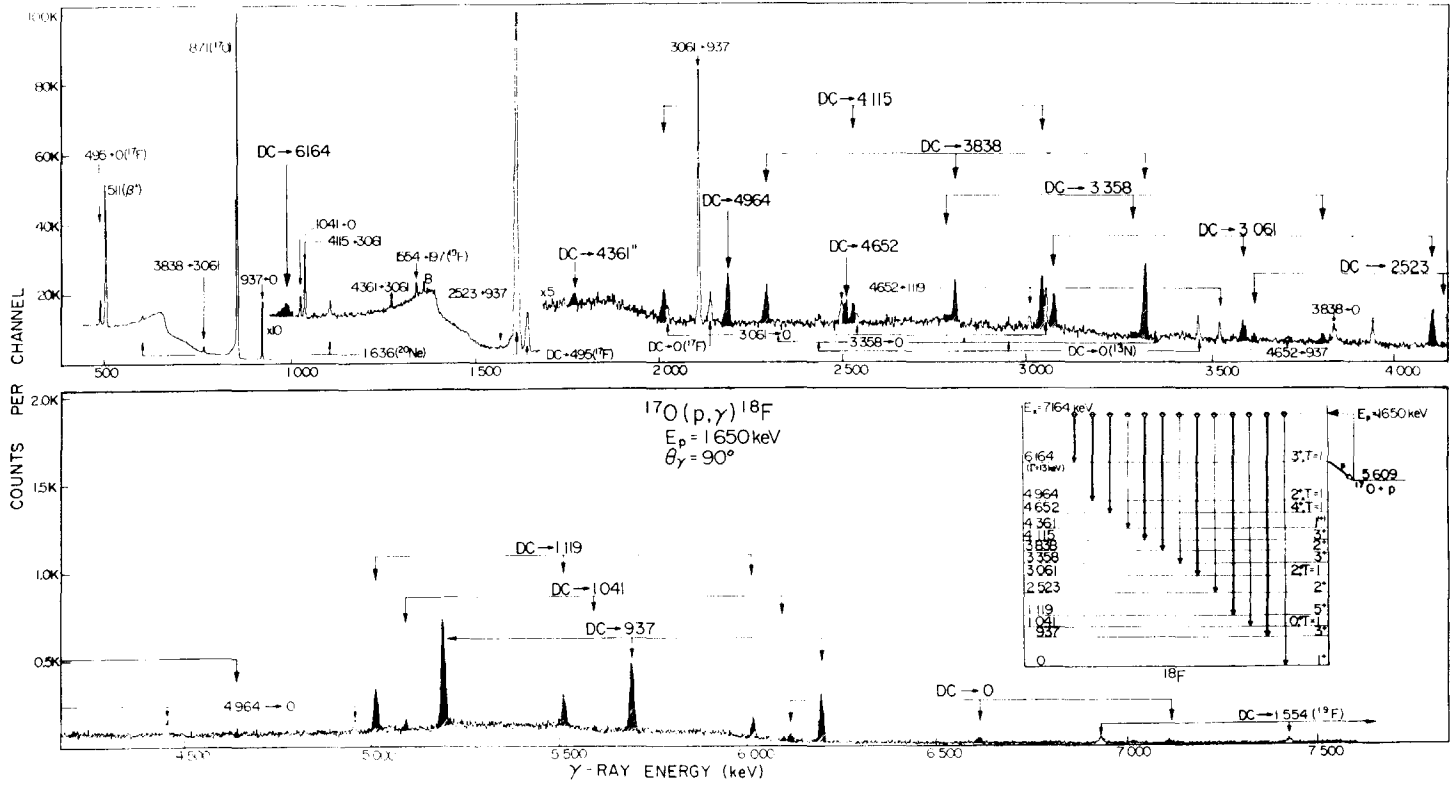

Fig. 10. Sample non-resonant γ-ray spectrum of the reaction $^{17}O(p,\gamma)^{18}F$ as obtained at $\vartheta_\gamma = 90°$ and $E_p = 1650$ keV with the 50 cm^3 Ge(Li) detector at $D = 8$ cm. The 8 keV WO_3 target (on W backing) was 90% enriched in ^{17}O. The primary direct-capture γ-rays are cross-hatched and identified as shown in the inset level diagram. The most intense contaminant γ-rays are due to the residual percentage of ^{16}O and ^{18}O in the target.

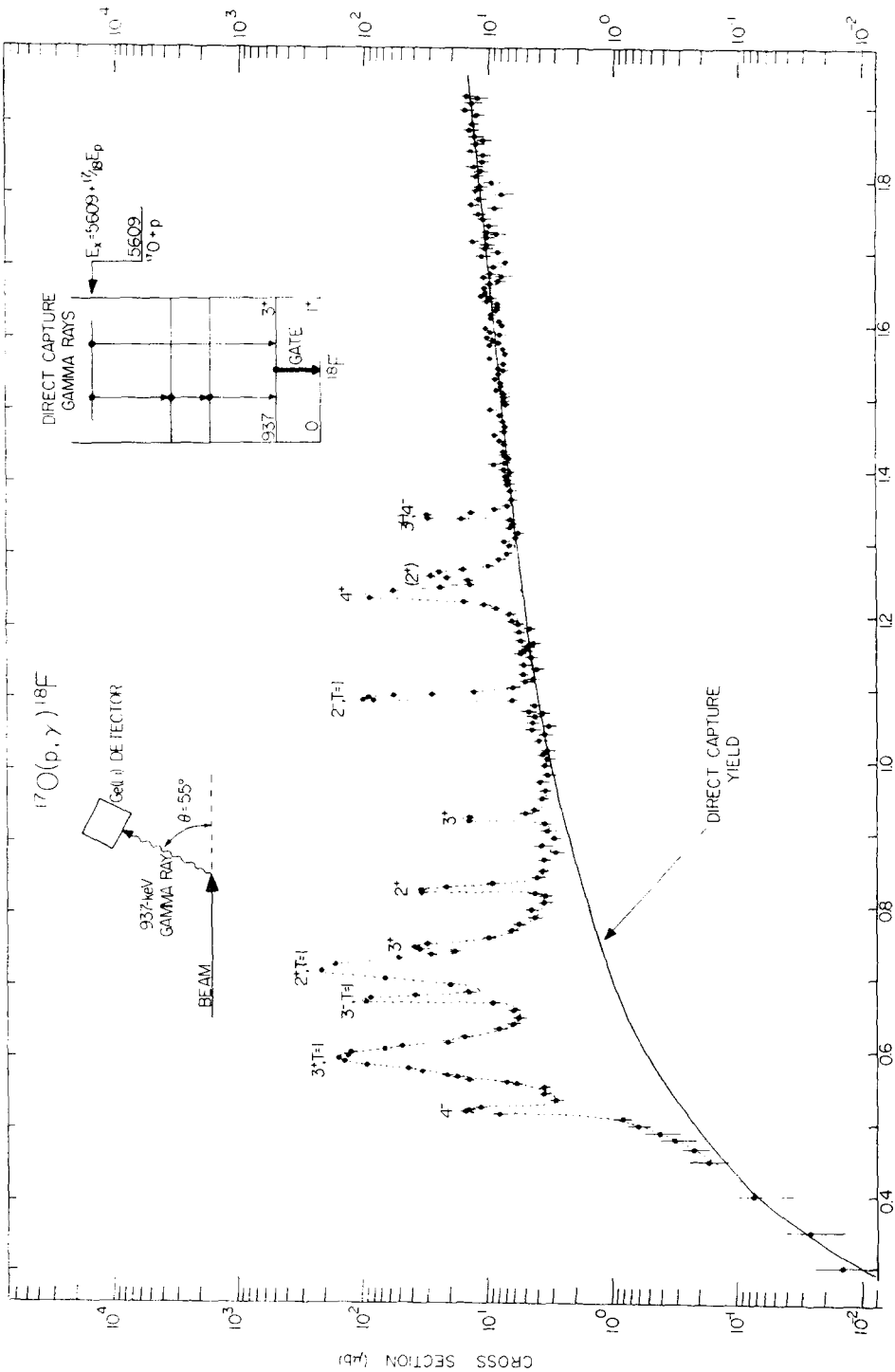

Fig. 11. Yield curve for the 0.94 → 0 MeV γ-ray transition in ^{18}F for the ^{17}O(p,γ)^{18}F reaction at $\theta_\gamma = 55°$ and $E_p = 0.3$–1.9 MeV. The observed resonances in the reaction are labelled by their reported (J^π, T) assignments [31]. The solid line through the data points represents the energy dependence of the non-resonant yield as predicted by the direct capture model.

configuration, and can only be formed directly through small $(d_{\frac{5}{2}})^2$ admixtures. Furthermore, the direct capture process should shine light on possible (2p-0h) admixtures of the above types in the proposed (4p-2h) states of the $K^\pi = 1^+$ rotational band (fig. 9). The low-lying negative-parity states can be populated through (2p-0h) admixtures of the type $(d_{\frac{5}{2}}, f_{\frac{5}{2},\frac{7}{2}})$ or $(d_{\frac{5}{2}}, p_{\frac{1}{2},\frac{3}{2}})$ in the predominantly (3p-1h) states (fig. 9).

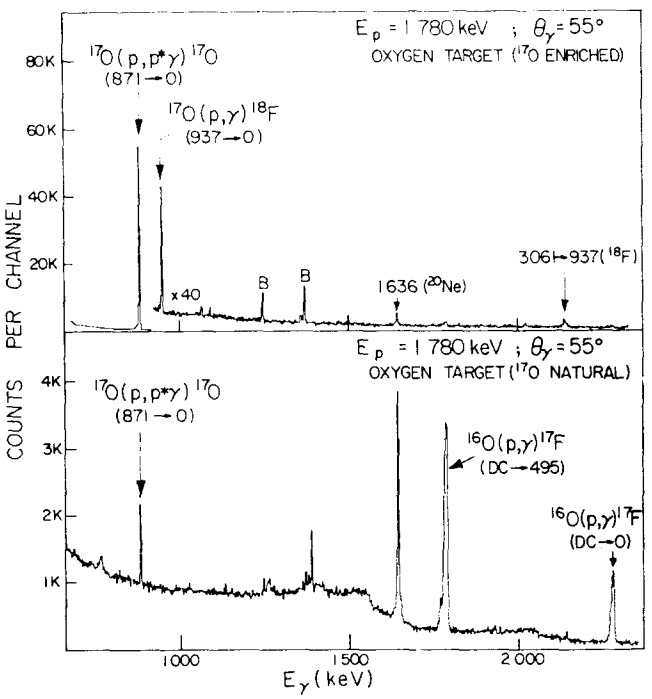

Fig. 12. Sample γ-ray spectra obtained at $E_p = 1780$ keV and $\theta_{\gamma'} = 55°$ by proton bombardment of an oxygen target (a) enriched in ^{17}O and (b) with natural ^{17}O abundance.

A sample "off-resonance" γ-ray spectrum of the $^{17}O(p, \gamma)^{18}F$ reaction is shown in fig. 10. As expected from the discussion above, non-resonant γ-ray transitions to all the (2p-0h) states up to $E_x = 6.16$ MeV have been observed along with weak branches to the (4p-2h) states at 2.52 and 3.36 MeV. The observed branching ratios, as deduced at $E_p = 1625$ keV, are listed in table 2. For a preliminary identification of these non-resonant transitions as due to the direct capture process, a detailed yield curve over a wide range of beam energy was first performed for the $0.94 \rightarrow 0$ MeV secondary γ-ray transition, since its intensity represents $\approx 70\%$ of the non-resonant γ-ray yield (fig. 10) through direct feed as well as γ-γ cascades from higher states. A yield, slowly varying with beam energy, is observed (fig. 11) upon which the various known resonances [31]) of the reaction are superposed. The energy dependence

of the smooth yield for $E_p < 400$ keV and $E_p > 1000$ keV is well reproduced by the calculations based on the direct-capture model †. These results encouraged more detailed studies of the observed non-resonant transitions, which are described in the following subsections.

TABLE 2

Branching ratios and absolute cross sections for $^{17}O(p,\gamma)^{18}F$ at $E_p = 1625$ keV

Transition (MeV)	J_f^π	Branching ratios [a]) (%)	Total cross sections [b]) (μb)
DC → 0	1^+	3.6±0.4	0.37±0.04
DC → 0.94	3^+	34.0±4.0	3.57±0.4
DC → 1.04	$0^+, T = 1$	1.6±0.3	0.16±0.03
DC → 1.08	0^+	< 0.5	< 0.05
DC → 1.20	5^+	16.6±1.3	1.74±0.14
DC → 1.70	1^+	< 0.3	< 0.03
DC → 2.10	2^-	< 0.9	< 0.10
DC → 2.52	2^+	1.7±0.4	0.12±0.03
DC → 3.06	$2^+, T = 1$	9.6±0.9	1.00±0.10
DC → 3.13	1^-	< 0.3	< 0.03
DC → 3.36	3^+	2.0±0.5	0.21±0.05
DC → 3.73	1^+	< 1.0	< 0.10
DC → 3.79	3^-	< 0.5	< 0.05
DC → 3.84	2^+	10.0±1.0	1.04±0.10
DC → 4.12	3^+	7.6±1.1	0.81±0.11
DC → 4.23	$2^{(-)}$	< 1.0	< 0.10
DC → 4.36	$1^{(+)}$	0.2±0.1	0.02±0.01
DC → 4.40	4^-	< 0.1	< 0.01
DC → 4.65	$4^+, T = 1$	3.7±0.6	0.39±0.06
DC → 4.75	$(0^+, T = 1)$	< 0.1	< 0.01
DC → 4.86	$1^{(-)}$	< 0.5	< 0.05
DC → 4.96	$2^+, T = 1$	4.8±0.5	0.49±0.05
DC → 5.30	4^+	< 0.2	< 0.02
DC → 6.14	$0^+, T = 1$	< 0.1	< 0.01
DC → 6.16	$3^+, T = 1$	4.6±0.5	0.48±0.05

[a]) Normalized to 100%. The branching ratios change very little with beam energy (figs. 13–15).
[b]) Relative to the well-known $^{16}O(p,\gamma)^{17}F$ cross section. The errors are subject to an additional 18% uncertainty in the relative cross-section measurement (subsect. 4.2.2).

4.2.2. Cross section measurement. The cross section for the direct-capture yield was measured with a method which compares directly the cross section for $^{17}O(p,\gamma)^{18}F$ with the well-known cross section for $^{16}O(p,\gamma)^{17}F$ (subsect. 4.1). This method avoids the usual difficulties associated with either absolute measurements or measurements relative to resonances [31, 48]).

Through the intermediary of the 0.87 → 0 MeV γ-ray transition from the $^{17}O(p,p^*)^{17}O$ reaction, the yield of the non-resonant γ-ray transitions from the $^{17}O(p,\gamma)^{18}F$ reaction were related to those from the $^{16}O(p,\gamma)^{17}F$ reaction. Fig. 12

† Hard-sphere phase shifts were again used for the nuclear phase shifts δ_{l_i} (subsect. 2.2).

illustrates two γ-ray spectra obtained, at the same beam energy and angle of observation, with natural oxygen and enriched ^{17}O targets. The $0.94 \rightarrow 0$ MeV secondary γ-ray transition from $^{17}O(p, \gamma)^{18}F$ was related to the DC $\rightarrow$ 0.50 MeV γ-ray transition from $^{16}O(p, \gamma)^{17}F$ through the equation:

$$\sigma(0.94 \rightarrow 0) = R \frac{r(^{16}O)}{r(^{17}O)} \frac{\varepsilon_\gamma(DC \rightarrow 0.50)}{\varepsilon_\gamma(0.94 \rightarrow 0)} \sigma(DC \rightarrow 0.50). \quad (17)$$

The ratio $r(^{16}O)/r(^{17}O)$ represents the well-known natural abundance ratio [58]) of $^{16}O(99.759\%)$ to $^{17}O(0.037\%)$, $\varepsilon_\gamma(DC \rightarrow 0.50)/\varepsilon_\gamma(0.94 \rightarrow 0)$ is the ratio of the relative detection efficiencies and R is the γ-ray intensity ratio given by

$$R = \left(\frac{I_\gamma(0.94 \rightarrow 0)}{I_\gamma(0.87 \rightarrow 0)}\right)_{\text{enriched}} \times \left(\frac{I_\gamma(0.87 \rightarrow 0)}{I_\gamma(DC \rightarrow 0.50)}\right)_{\text{natural}}.$$

Eq. (17) is justified when the yield curves for all three reactions are smooth within the energy range of the target thickness. This condition is well fulfilled for the two capture reactions at the beam energy used (figs. 7 and 11) and has also been tested for the $^{17}O(p, p^*)^{17}O$ reaction. The resulting absolute cross section of $\sigma = 10.7 \pm 1.9$ μb for the 0.94 $\rightarrow$ 0 MeV secondary γ-ray transition in the $^{17}O(p, \gamma)^{18}F$ reaction at $E_p = 1780$ keV was then used to obtain the corresponding values for the primary transitions quoted in table 2.

4.2.3. The direct-capture transitions. A study of the properties of the direct-capture γ-ray transitions (fig. 10 and table 2) is complicated below $E_p = 900$ keV due to the presence of strong resonances, especially the two broad resonances [31, 35]) at $E_p = 587$ and 714 keV (fig. 11). Below $E_p = 400$ keV, the direct-capture cross section is two orders of magnitude reduced. These transitions, therefore, have only been studied in detail in the energy range $E_p = 900$–1750 keV. The resulting yield curves obtained concurrently at $\vartheta_\gamma = 0°$ and 90° are illustrated in figs. 13–15. The yield of all γ-rays follows a smooth curve, interrupted by a few sharp resonances. The DC $\rightarrow 0(1^+)$ γ-ray yield is exceptional in that a broad interfering resonance occurs in this region (fig. 13). The angular distributions for the transitions obtained at $E_p = 1625$ keV are included in figs. 13–15.

The direct-capture transitions can, for the purpose of a more detailed discussion, be grouped into two classes:

(i) Final states which have only an $l_f = 2$ final orbital angular momentum i.e. states with configurations of the type $(d_{\frac{5}{2}}, d_{\frac{5}{2}})$ or $(d_{\frac{5}{2}}, d_{\frac{3}{2}})$. These are the states at $E_x(J^\pi) = 0(1^+)$, $1.04(0^+)$, $1.12(5^+)$, $4.36(1^+)$ and $4.65(4^+)$ MeV. The yield curves as well as the angular distributions for the transitions to all these states (fig. 13) are consistent with the direct-capture picture for $l_f = 2$ (subsects. 2.3.1 and 4.1). The DC $\rightarrow 0(1^+)$ transition is obscured over a wide region of beam energies by interference with the broad ($\Gamma \approx 90$ keV) 2^- resonance [31]) at $E_p = 1274$ keV (subsect. 4.2.5.). The direct capture process seems however to dominate the yield curve at $E_p > 1600$ keV. This is indicated by the increasing anisotropy between 0°

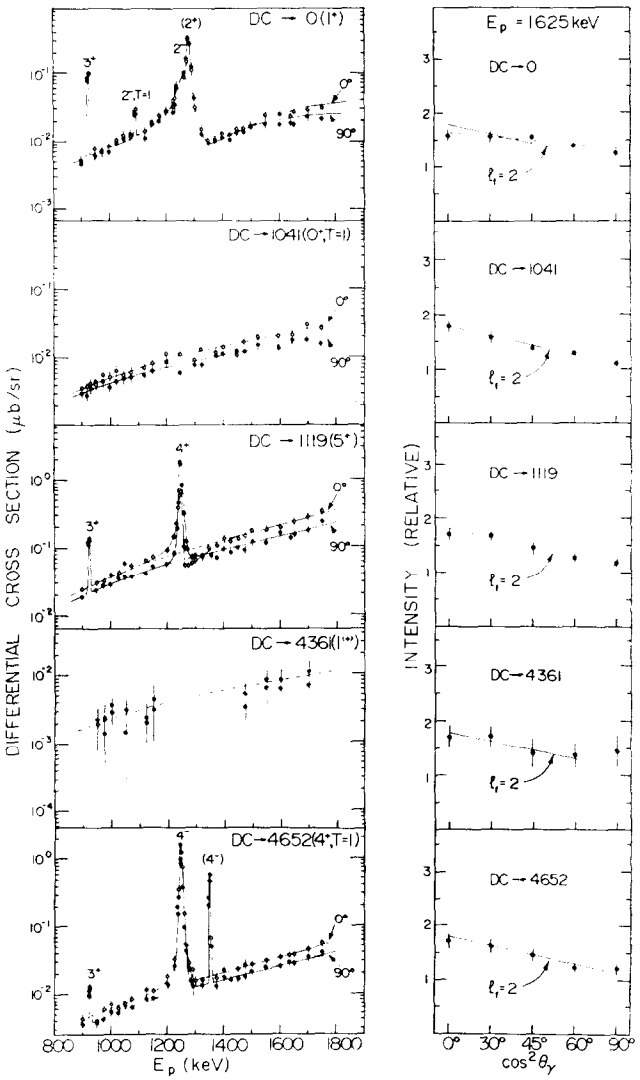

Fig. 13. Yield curves for direct-capture γ-ray transitions to states in ^{18}F observed in the ^{17}O(p,γ)^{18}F reaction. The solid (dashed) lines through the data points are the calculated yield curves. The weak cross section for the DC $\rightarrow$ 4.36(1$^{(+)}$) MeV transition did not allow a reliable yield curve in the resonance region at $E_p \approx$ 1.2–1.4 MeV. Also shown are angular distributions obtained at E_p = 1625 keV. The solid lines through the data points are the model predictions for the assumed final orbital angular momentum l_f.

and 90°, expected from the direct capture model. The spectroscopic factors $C^2S(l = 2)$ deduced for these states are compared with available stripping data [39]) in table 3. Excellent agreement is noted. The corresponding values from shell-model

TABLE 3

Comparison of experimental and theoretical spectroscopic factors, $C^2S(l)$, for positive parity states in ^{18}F

State (MeV)	J^π	Experimental				Theory					
		Direct capture $^{17}O(p,\gamma)^{18}F$		Stripping [39] $^{17}O(\tau, d)^{18}F$		K+B [32]		B+F [43]		E+E [44]	
		$l=0$	$l=2$	$l=0$	$l=2$	$l=0$	$l=2$	$l=0$	$l=2$	$l=0$	$l=2$
0	1^+		0.50		0.62		0.57		0.56		0.43
0.94	3^+	0.50	0.53	≈ 0.26	< 0.30	0.33	0.30	0.21	0.38	0.27	0.24
1.04	$0^+, T=1$		0.78		0.96		0.83		0.81		0.68
1.12	5^+		0.78		0.83		1.00		0.89		0.81
1.70	1^+		< 0.10		[a]		[b]		0.046		10^{-4}
2.52	2^+	0.021	0.039	≈ 0.02	< 0.004		[b]	8×10^{-4}	1.4×10^{-4}	0.03	0.01
3.06	$2^+, T=1$	0.22	0.61	0.13	0.61	0.19	0.56	0.14	0.61	0.15	0.51
3.36	3^+	0.04	0.05	[a]	[a]		[b]	0.016	0.055	10^{-4}	10^{-3}
3.73	1^+		< 0.50		[a]		0.27		0.20		0.27
3.84	2^+	0.34	0.27	0.35–0.48	< 0.47	0.25	0.16	0.21	0.02	0.21	0.10
4.12	3^+	0.20	0.44	0.11	0.63	0.16	0.65	0.21	0.55	0.13	0.56
4.36	$1^{(+)}$		0.11		[a]		0.35		0.08		[a]
4.65	$4^+, T=1$		0.77		0.81		0.95		0.96		0.81
4.75	$(0^+, T=1)$		< 0.21		[a]		[b]		0.063		[a]
4.96	$2^+, T=1$	0.18	0.37	0.18	0.41	0.28	0.42	0.26	0.38	0.23	0.31
5.30	4^+		< 0.10		[a]		[b]		0.0		[a]
6.14	$0^+, T=1$		< 0.28 [c]		[a]		0.09		0.094		[a]
6.16	$3^+, T=1$	0.49 [c]	< 0.05 [c]	[a]	[a]	0.50	2×10^{-4}	0.50	0.0		[a]

[a] Not reported.
[b] Outside model space used.
[c] Bound-state formalism assumed (subsect. 4.2.3).

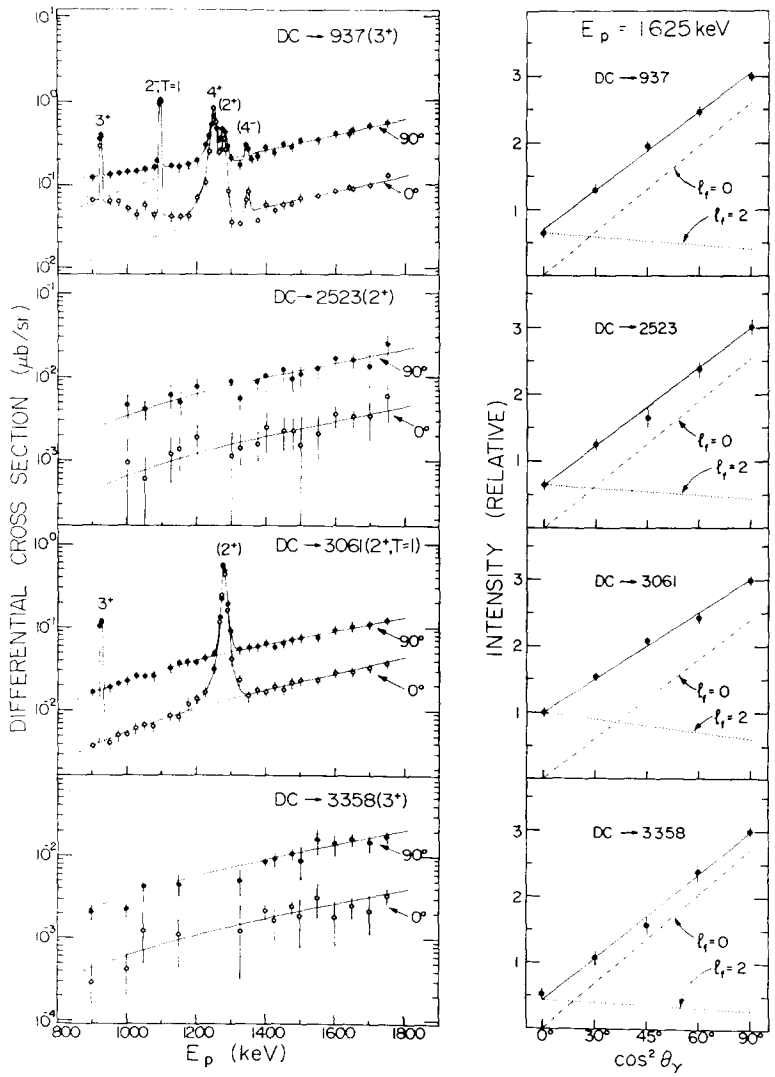

Fig. 14. Yield curves for direct-capture γ-ray transitions to the 0.94, 2.52, 3.06 and 3.36 MeV states in ^{18}F observed in the ^{17}O(p,γ)^{18}F reaction. The solid (dashed) lines through the data points are the model predictions. Also shown are angular distributions obtained at $E_p = 1625$ keV. The angular distributions have been decomposed into their $l_f = 0$ and $l_f = 2$ components (dashed and dotted lines).

calculations of Kuo and Brown [32]) (K+B), Benson and Flowers [43]) (B+F) and Ellis and Engeland [44]) (E+E) have been calculated with the relation [39])

$$C^2S(l = 2) = C^2\{2\alpha^2(d_{\frac{5}{2}}, d_{\frac{5}{2}}) + \beta^2(d_{\frac{5}{2}}, d_{\frac{3}{2}})\}, \tag{18}$$

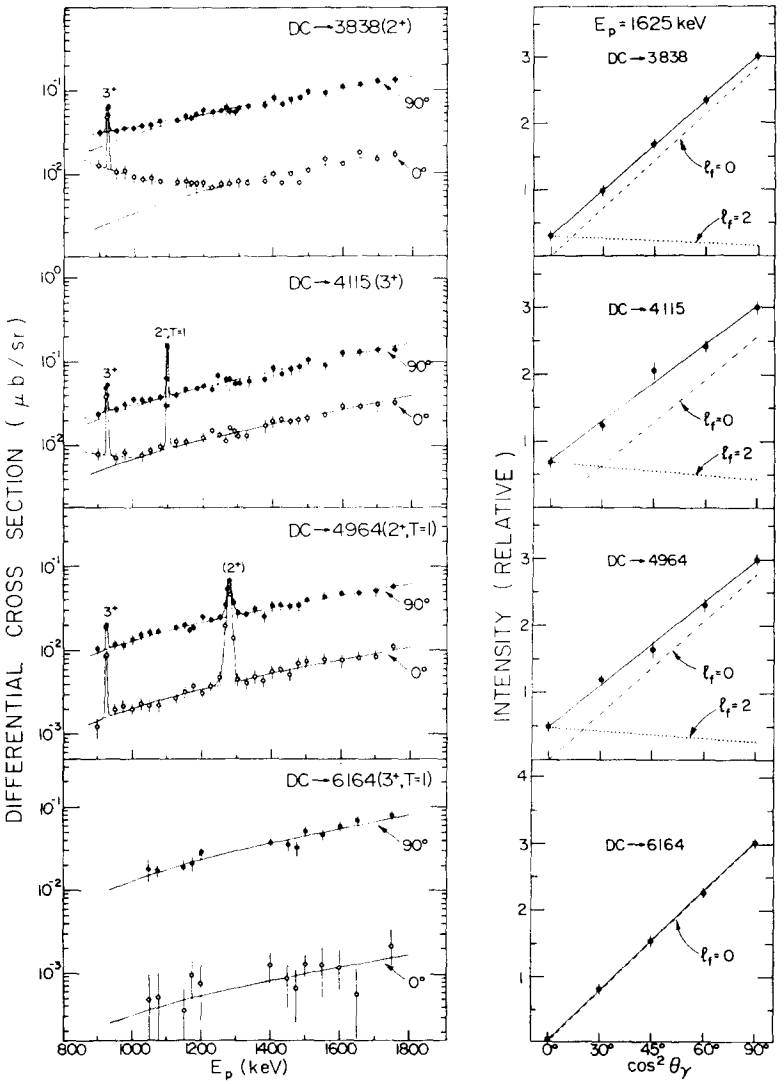

Fig. 15. Yield curves for direct-capture γ-ray transitions to the 3.84, 4.12, 4.96 and 6.16 MeV states in ^{18}F observed in the ^{17}O(p,γ)^{18}F reaction. The solid (dashed) lines through the data points are the model predictions. Also shown are angular distributions obtained at $E_p = 1625$ keV. The angular distributions have been decomposed into their $l_f = 0$ and $l_f = 2$ components (dashed and dotted lines).

where α and β are the expansion coefficients obtained from the shell-model calculations. Good overall agreement is noted, supporting therefore the previously proposed model identifications [32, 35]) of these states.

(ii) Final states which contain, in addition to the configurations $(d_{\frac{5}{2}}, d_{\frac{5}{2}})$ or $(d_{\frac{5}{2}}, d_{\frac{3}{2}})$, a third configuration $(d_{\frac{5}{2}}, s_{\frac{1}{2}})$. These are the states with $J^\pi = 2^+$ or 3^+,

namely the states at $E_x(J^\pi) = 0.94(3^+)$, $2.52(2^+)$, $3.06(2^+)$, $3.36(3^+)$, $3.84(2^+)$, $4.12(3^+)$, $4.94(2^+)$ and $6.16(3^+)$ MeV. The yield curves at 0° and 90° and the angular distributions, obtained at $E_p = 1625$ keV, are shown in figs. 14 and 15. All these results are consistent with the model calculations for the appropriate mixtures of $l_f = 0$ and $l_f = 2$. Apparent exceptions are the yield curves for the DC → 0.94, DC → 3.84 and DC → 4.12 MeV transitions for $E_p < 1200$ keV. These deviations can be accounted for by contributions of the high-energy tails of the two broad resonances at $E_p = 587$ and 714 keV. The strongest γ-ray branches of these two resonances proceed to the three states mentioned above [31]). The observed anisotropies for the transitions to all these states reveal an $l_f = 0$ orbital momentum in their wave functions i.e. $(d_{\frac{5}{2}}, s_{\frac{1}{2}})$ components. These angular distributions can be decomposed into the contributions from the $l_f = 0$ and $l_f = 2$ components (subsect. 2.3.1 and sect. 3). The spectroscopic factors deduced for the $l_f = 0$ and $l_f = 2$ components are presented in table 3 and compared with stripping data. In general, good agreement is found. The corresponding spectroscopic factors from shell-model wave functions were deduced for the $l_f = 2$ components as described above, and for the $l_f = 0$ component [39]) by

$$C^2S(l = 0) = C^2\gamma^2(d_{\frac{5}{2}}, s_{\frac{1}{2}}), \tag{19}$$

where γ is the predicted expansion coefficient in the wave function. Fair agreement is noted, thus supporting the model identification of the states shown in fig. 9.

It should be mentioned here that the quoted spectroscopic factors for the 6.14 and 6.16 MeV states in table 3 are obtained by the assumption that these states are just bound. The calculation of the direct capture cross section for these unbound states involves a radial integral containing two Coulomb distorted plane waves in the asymptotic region which is difficult to calculate in a straightforward manner. Since the direct-capture transitions to these unbound states are closely related to the "nuclear bremsstrahlung", one can by analogy with bremsstrahlung theory resolve the above difficulty as pointed out by Faessler [21]). No attempt has been made in the present work to proceed along this line for the two states mentioned above.

The upper limits of the spectroscopic factors for "unobserved" transitions to the other low-lying positive parity states (table 3) are useful numbers since they provide limits for the admixtures in the proposed configurations.

No direct-capture γ-ray transitions have been observed to the low-lying negative parity states in ^{18}F, in agreement with the previously proposed (3p-1h) configuration of these states. The upper limits for the spectroscopic factors of the states given in table 2 are $C^2S(l_f = 1) \lessapprox 0.05$ and $C^2S(l_f = 3) \lessapprox 0.10$. Recent shell-model calculations [40]) predict these low-lying negative parity states to have, on the average, a (2p-0h) admixture of $< 10\%$.

Finally, in concluding this section, it is worthwhile to point out two important features of the direct capture γ-ray angular distributions:

(a) These angular distributions as demonstrated by the results for transitions within

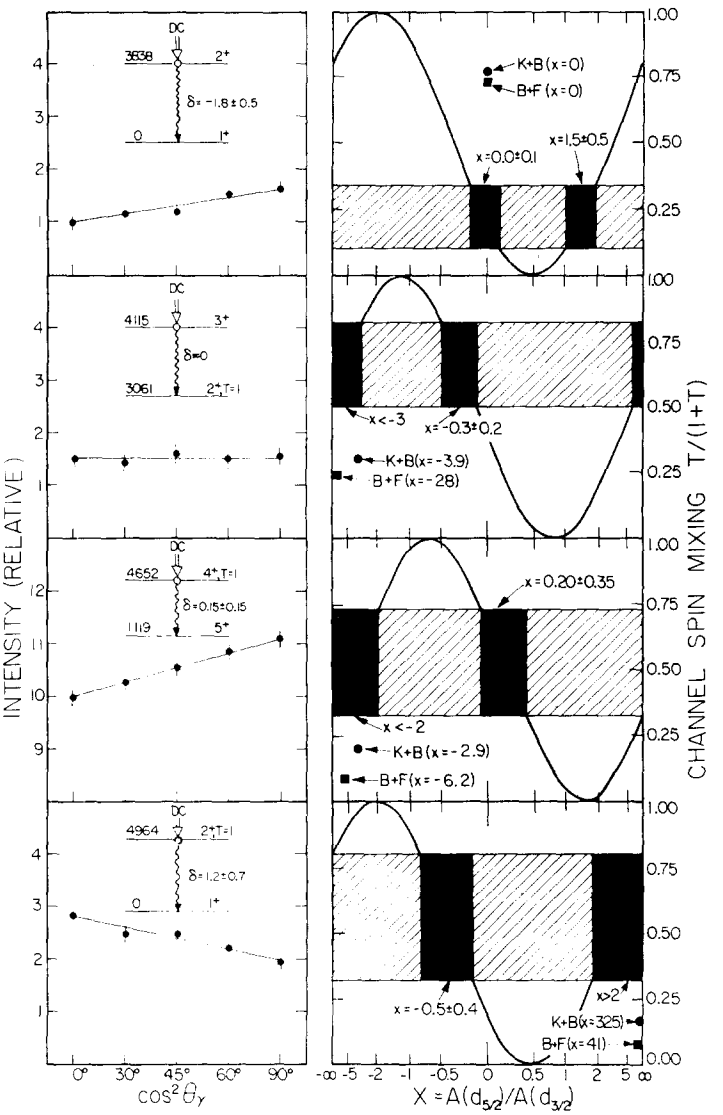

Fig. 16. Angular distributions for secondary transitions from states populated through the direct-capture process. The analysis of these data in terms of $d_{\frac{5}{2}}$ and $d_{\frac{3}{2}}$ components in the captured states are also included (for details see text).

class 1 (see above and fig. 13) are independent of the total angular momentum J_f of the final state and thus, as predicted, depend only on l_f (subsect. 2.3.1).

(b) In view of the previously observed isotropy or near isotropy for the γ-ray angular distributions in resonances (with $J \leqq 3$) due to the high spin of the target nucleus [refs. [32, 34, 35]) and figs. 14 and 15], the observation of large anisotropies away from resonances is a striking feature. This feature clearly demonstrates the strong

presence of the direct-capture process. These results combined with those for the $^{16}O(p, \gamma)^{17}F$ reaction (subsect. 4.1) confirm therefore the predicted independence of the direct-capture angular distributions on the spin of the target nucleus (subsect. 2.3.1).

4.2.4. The secondary transitions. The yield curves for the secondary transitions show the same general features as those for the primary transitions. An example is illustrated in fig. 11 for the 0.94 → 0 MeV transition. A detailed analysis of the angular distributions for the secondary transitions in terms of the j-values associated with the final orbital angular momenta l_f (subsect. 2.3.2) was attempted only for the states at 3.84, 4.12, 4.65 and 4.96 MeV. Since the lower-lying states are also populated via γ-cascades from higher states, the analysis is more complicated and has not yet been attempted.

For direct capture to the $4.65(4^+)$ MeV state, formed with $l_f = 2$ only (fig. 13), the amplitude ratio of the configurations $d_{\frac{3}{2}}$ and $d_{\frac{5}{2}}$ in the 4.65 MeV final-state wave function, $x = A(d_{\frac{5}{2}})/A(d_{\frac{3}{2}})$, can be deduced from the angular distribution of the secondary γ-ray transition 4.65 → 1.12 MeV (fig. 16) with the aid of the eqs. (14) and (15) [subsect. 2.3.2] and $\delta(4.65 \rightarrow 1.12) = 0.15 \pm 0.15$ [ref. [34])]. In this analysis, the ratios x and t (channel spin intensity ratio) are related by eq. (16) [subsect. 2.3.2] which reduces to $t = (\sqrt{2}-x)^2/(1+\sqrt{2}x)^2$. The dependence of the function $t/(1+t)$ on x is shown as a solid line in fig. 16 and together with the experimental value of $t/(1+t) = 0.5 \pm 0.2$ (cross-hatched area), two solutions for x are found (black area): $x < -2$ and $x = 0.20 \pm 0.35$. These ambiguities cannot be resolved with these techniques but nevertheless the two values for x may be compared with theoretical predictions. For the 4.65 MeV state, both the K+B and B+F models predict x in the region of the first solution (fig. 16), i.e. predominant $d_{\frac{5}{2}}$ capture.

The angular distributions of the secondary transitions from the 3.84, 4.12 and 4.96 MeV states contain large isotropic components due to the $l_f = 0$ components in their wave functions (fig. 15 and subsect. 2.3.2). The magnitudes of the isotropic components were determined from the results of the primary transitions (fig. 15). After the subtraction of this component, the resulting angular distributions of the secondary transitions for the remaining $l_f = 2$ components were analyzed with respect to $x = A(d_{\frac{5}{2}})/A(d_{\frac{3}{2}})$ in the way described above. For these three states, the channel spin ratio is given by the expressions

$$t(3.84 \text{ and } 4.96) = \left(\frac{1-2x}{2+x}\right)^2, \qquad t(4.12) = \left(\frac{\sqrt{2}-\sqrt{3}x}{\sqrt{3}+\sqrt{2}x}\right)^2.$$

The values of x derived from the experimental results are shown in fig. 16. The corresponding shell-model predictions of K+B and B+F are also shown in fig. 16 and are consistent with one of the experimental values.

4.2.5. Information on resonances. The values of $\omega\gamma = (2J+1)\Gamma_p\Gamma_\gamma/\Gamma$ for the resonances in the $^{17}O(p, \gamma)^{18}F$ reaction were previously determined [31]) relative to the $\omega\gamma$ value of the $E_p = 633$ keV resonance in $^{27}Al(p, \gamma)^{28}Si$. In the present work,

independent values for $\omega\gamma$ in the $^{17}O(p,\gamma)^{18}F$ reaction have been determined by comparison with the direct-capture cross sections. For example, a value of $\omega\gamma = 3.8\pm0.7$ eV for the $E_p = 1094$ keV resonance was obtained, in excellent agreement with the reported value [31]) of $\omega\gamma = 4.2\pm1.2$ eV.

The branching ratios from the present work for the resonances in the region $E_p = 0.9$–1.7 MeV are consistent with previous results with the exceptions that two new weak branches were established:

(i) For the $E_p = 1094$ keV resonance a value of $0.20\pm0.05\%$ has been found for the $R \rightarrow 0$ transition (fig. 13) compared with the previous upper limit [34]) of $< 0.3\%$.

(ii) For the $E_p = 1345$ keV resonance the R $\rightarrow$ 0.94 MeV transition was observed (fig. 14) to be $1.5\pm0.5\%$ compared with the reported upper limit [34]) of $< 1.8\%$.

The yield curves at 0° and 90° for the DC $\rightarrow$ 0 transition around $E_p = 1.3$ MeV exhibit the same structure (fig. 13) indicating an a_0 interference term. This feature requires the interfering amplitudes to be of the same spin and parity (appendix A.3). Since the DC $\rightarrow$ 0 transition arises from the process E1(p/f $\rightarrow$ d), the interfering resonance must also be formed through p (or f) wave formation. This is consistent with the $J^\pi = 2^-$ assignment for the broad resonance ($\Gamma \approx 90$ keV) reported [59]) at $E_p = 1274$ keV.

For the DC $\rightarrow$ 1.12 MeV transition in the region of the $J^\pi = 4^+$ resonance ($E_p = 1240$ keV), a normal resonance yield curve at 90° has been observed but the 0° yield curve showed a pronounced interference term (fig. 13). This structure can be explained as the interference between the resonance amplitude [mainly d-wave [35])] and the direct-capture amplitude (p- or f-wave) resulting in an a_1 dependence of the differential yield curves.

5. Astrophysical *S*-factor

The direct-capture process is of astrophysical interest since its cross section, when integrated over energy, is in many cases much larger than any of the cross sections of the individual resonances in the reaction. If the energy variation of the experimental cross section is satisfactorily reproduced by the direct-capture model over a wide range of beam energies, a reliable extrapolation of the cross section to stellar energies can be made. Since the capture cross section for low bombarding energies decreases rapidly, the cross section is usually expressed in terms of the astrophysical *S*-factor defined [54, 55]) by

$$\sigma_{tot} = S e^{-2\pi\eta}/E_{c.m.}, \tag{20}$$

where η is the usual Coulomb parameter and $E_{c.m.}$ the projectile energy in the c.m. system. From the data presented in sect. 4, the *S*-factors have been deduced from the total cross sections (sum of all direct capture transitions to bound states) and eq. (20), and extrapolated to stellar energies via the direct-capture model. The results for the $^{16}O(p,\gamma)^{17}F$ and $^{17}O(p,\gamma)^{18}F$ reactions are shown in fig. 17.

The reaction $^{16}O(p, \gamma)^{17}F$ is of interest in the CNO cycle [54, 55]). The loss of CN catalyst from the main CN cycle through the reaction $^{15}N(p, \gamma)^{16}O$ is replenished by the sequence of reactions

$$^{16}O(p, \gamma)^{17}F(\beta+\nu)^{17}O(p, \alpha)^{14}N.$$

If the reaction $^{17}O(p, \alpha)^{14}N$ is fast at stellar energies, then the loss of catalyst would be counteracted at a rate determined by the $^{16}O(p, \gamma)^{17}F$ reaction. The speed of the $^{17}O(p, \alpha)^{14}N$ reaction depends on the suggested existence [61]) of a resonance at $E_p = 65$ keV ($J^\pi = 1^-$ state at $E_x = 5.67$ MeV in ^{18}F) with a reduced proton width of $\theta_p^2(l = 1) \approx 0.01$. If the actual value for θ_p^2 is smaller by 2 or 3 orders of magnitude,

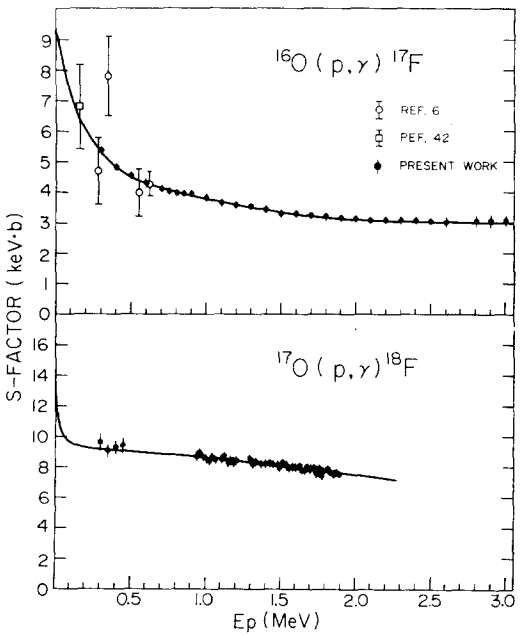

Fig. 17. Astrophysical S-factor for the reactions $^{16}O(p,\gamma)^{17}F$ and $^{17}O(p,\gamma)^{18}F$ from present and previous work. The solid lines through the data points represent the direct-capture model calculations. The relative errors for the present work are as indicated but are subject to the additional 18% error of the absolute cross section used as the standard (subsect. 4.2.2).

the speed of the above side cycle would be determined by this latter reaction rather than the $^{16}O(p, \gamma)^{17}F$ reaction. However, since the S-factor for the $^{17}O(p, \gamma)^{18}F$ reaction is, at all beam energies, larger than that for the $^{16}O(p, \gamma)^{17}F$ reaction (fig. 17), an alternative side cycle can be proposed whose speed may still be determined by the $^{16}O(p, \gamma)^{17}F$ reaction:

$$^{16}O(p, \gamma)^{17}F(\beta+\nu)^{17}O(p, \gamma)^{18}F(\beta+\nu)^{18}O(p, \alpha)^{15}N.$$

The high level density [59]) at $E_x = 8$ MeV in ^{19}F ($\approx$ five states at $E_x = 7.9$–8.1 MeV with $\Gamma = 5$–260 keV) would probably guarantee that the last reaction $^{18}O(p, \alpha)^{15}N$

is fast. A measurement of the cross sections for $^{17}O(p, \alpha)^{14}N$ and $^{18}O(p, \alpha)^{15}N$ at low beam energies is therefore desirable.

6. Summary

It has been demonstrated that the direct radiative capture process for protons can be used to provide detailed nuclear structure information:

(i) The angular distributions of the direct-capture γ-rays are characterized by the orbital angular momenta l_f involved in the final states. Information on the j-values of these captured orbits ($j = l_f \pm \frac{1}{2}$ for proton capture) can be obtained from the secondary transitions. The necessary experimental data are provided concurrently with the data for the primary (direct-capture) transitions.

(ii) A comparison of predicted and observed cross sections yields spectroscopic factors for final states.

In all cases studied, good agreement with stripping data was noted. After refinements of the direct-capture model (see below) it should be possible to make a more detailed comparison between the information obtained from stripping and direct-capture reactions. The attraction of the direct-capture reaction lies however in the simplicity of the reaction mechanism in conjunction with the well-known electromagnetic interaction. Furthermore, spectroscopic factors for final bound states produced by the capture of more complex particles e.g. ^4He could be deduced from the direct-capture model. In comparison, the theory for α-particle transfer reactions is quite complex and as a consequence reliable spectroscopic factors from such data are not yet available.

It appears that the simple two-body direct-capture model (sect. 2) can be used to explain a large variety of experimental data over a wide range of beam energies. An important refinement of the model would involve the use of a Woods-Saxon potential including a spin-orbit term rather than the simple square-well potential.

The author thanks A. E. Litherland, K. P. Jackson, R. E. Azuma and A. J. Ferguson for many stimulating discussions, suggestions and the encouragement during the course of this work. The assistance of T. Clifford during the early parts of this work is highly appreciated. The cooperation of P. Ashbaugh and the technical staff of McMaster University, Hamilton contributed to the success of this work. The calculations were performed on the IBM 370 computer centre at the University of Toronto. Partial financial support from the National Research Council of Canada is gratefully acknowledged.

Appendix

A.1. ANGULAR DISTRIBUTIONS FOR DIRECT CAPTURE TRANSITIONS

The angular distribution for an unpolarized γ-ray transition of multipole (L, M) between a state $|J_1 M_1\rangle$ and a state $|J_2 M_2\rangle$ is given by [26, 27])

$$W(\vartheta_1) = \sum_{M_1 M_2 P} |\sum_M \langle J_2 M_2 | T_{LM} | J_1 M_1 \rangle D^{(L)*}_{MP}(\vartheta_1, \varphi_1, 0)|^2$$
$$= \sum_{M_1 M_2 P} |\sum_M Q_{M_1 M M_2 P}|^2, \tag{A.1}$$

where T_{LM} represents the usual interaction multipole operator, which for electric transitions is proportional to the spherical harmonics $(-i)^L Y^M_L(\vartheta, \varphi)^*$, $D^{(L)}_{MP}(\vartheta_1, \varphi_1, 0)$ are elements of the rotation matrices and P is the circular polarization of the γ-radiation ($P = \pm 1$). Since $M = M_1 - M_2$, the summation over the transition matrix elements is incoherent and one index can be dropped:

$$W(\vartheta_1) = \sum_{M_1 M_2 P} |Q_{M_1 M_2 P}|^2. \tag{A.2}$$

In the following subsections, mainly angular distribution expressions for electric multipole transitions will be discussed (subsect. 2.1), but some expressions for M1 transitions will also be quoted.

A.1.1. Unique orbital angular momenta. The case for single-valued orbital angular momenta in both the initial and final states will be considered first. With the angular part of the wave functions of these states given (eqs. (5) and (6)) by

$$|J_1 M_1\rangle \propto \sum_{S_1} \hat{l}_1 \mathscr{Y}^0_{l_1}(\vartheta, \varphi) \chi^{M_1}_{S_1},$$
$$|J_2 M_2\rangle \propto \sum_{S_2 \beta} a_{S_2}(l_2\, M_2 - \beta\, S_2\, \beta | J_2 M_2) \mathscr{Y}^{M_2-\beta}_{l_2}(\vartheta, \varphi) \chi^{\beta}_{S_2}, \tag{A.3}$$

the transition matrix element becomes

$$Q_{M_1 M_2 P} \propto \sum_{S_1 S_2 \beta} a^*_{S_2} \hat{l}_1 (l_2\, M_2 - \beta\, S_2\, \beta | J_2 M_2) \langle \chi^{\beta}_{S_2} | \chi^{M_1}_{S_1} \rangle$$
$$\times \int \mathscr{Y}^{M_2-\beta}_{l_2}(\vartheta, \varphi)^* \mathscr{Y}^M_L(\vartheta, \varphi)^* \mathscr{Y}^0_{l_1}(\vartheta, \varphi) \mathrm{d}\Omega\, D^{(L)*}_{MP}(\vartheta_1, \varphi_1, 0). \tag{A.4}$$

This result can be reduced with the use of the relations

$$\langle \chi^{\beta}_{S_2} | \chi^{M_1}_{S_1} \rangle = \delta_{S_2 S_1} \delta_{\beta M_1}; (S_1 = S_2 = S), \tag{A.5}$$

$$\int \mathscr{Y}^{M_2-\beta *}_{l_2}(\vartheta, \varphi) \mathscr{Y}^{M*}_L(\vartheta, \varphi) \mathscr{Y}^0_{l_1}(\vartheta, \varphi) \mathrm{d}\Omega = \frac{1}{\sqrt{4\pi}} \hat{L} \hat{l}_1 \hat{l}_2^{-1} (l_1\, 0 L\, 0 | l_2\, 0)(l_1\, 0 L M | l_2\, M), \tag{A.6}$$

to give

$$Q_{M_1 M_2 P} \propto \sum_S a^*_S \hat{L} \hat{l}_1^2 \hat{l}_2^{-1} (l_2\, M_2 - M_1\, S M_1 | J_2 M_2)(l_1\, 0 L 0 | l_2\, 0)$$
$$\times (l_1\, 0 L M | l_2\, M) D^{(L)*}_{MP}(\vartheta_1, \varphi_1, 0). \tag{A.7}$$

The square of this expression can be evaluated with the help of the reduction formula for a product of rotation matrices [27])

$$D^{(L)*}_{MP} D^{(L)}_{MP} = (-)^{M+1} \sum_k (LPL\ -P|k0)(LML\ -M|k0) P_k(\vartheta_1), \tag{A.8}$$

and after an incoherent summing over the channel spin S [refs. [26, 27])], the angular distribution is given by

$$W(\vartheta_1) \propto \sum_{SkM_1M_2} |a_S|^2 \hat{L}^2 \hat{l}_1^4 \hat{l}_2^{-2} (l_2\, M_2 - M_1\, SM_1|J_2\, M_2)^2 (-)^{M+1}$$
$$\times (l_1\, 0L0|l_2\, 0)^2 (l_1\, 0LM|l_2\, M)^2 (L1L\ -1|k0)(LML\ -M|k0) P_k(\vartheta_1). \tag{A.9}$$

When the usual orthogonality relations for CG coefficients are used as well as the formula for products of CG coefficients in terms of Racah coefficients, the angular distribution becomes:

$$W(\vartheta_1) \propto \sum_k (-)^{l+k+l_2} \hat{l}_1^4 \hat{L}^2 \hat{l}_2^{-2} J_2^2 (l_1\, 0L0|l_2\, 0)^2 (l_1\, 0l_1\, 0|k0)$$
$$\times (L1L\ -1|k0) W(Ll_1\, Ll_1;\, l_2\, k) P_k(\vartheta_1). \tag{A.10}$$

With the definition [26])

$$\bar{Z}_1(l_1\, Ll_1\, L;\, l_2\, k) = (-)^{k+1} \hat{L}^2 \hat{l}_1^2 (L1L\ -1|k0) W(Ll_1\, Ll_1;\, l_2\, k) \tag{A.11}$$

the following result is obtained †:

$$W(\vartheta_1) = \sum_k (l_1\, 0l_1\, 0|k0) \bar{Z}_1(l_1\, Ll_1\, L;\, l_2\, k) P_k(\vartheta_1). \tag{A.12}$$

A.1.2. Mixed orbital angular momenta. If the final state contains contributions from more than one angular momentum l_2, its wave function including the radial dependence is given (eq. (6)) by

$$|J_2\, M_2\rangle = \sum_{l_2 S_2 \beta} a_{S_2} \frac{u_{l_2}(k_2\, r)}{r} (l_2\, M_2\ -\beta S_2\, \beta|J_2\, M_2) \mathscr{Y}^{M_2-\beta}_{l_2}(\vartheta, \varphi) \chi^{\beta}_{S_2}.$$

Similarly to the derivation of eq. (A.7), the transition matrix element is given here by

$$Q_{M_1M_2P} \propto \sum_{Sl_2} a^*_S (l_2\, M_2 - M_1\, SM_1|J_2\, M_2)(l_1\, 0L0|l_2\, 0)(l_1\, 0LM|l_2\, M) R_{l_1Ll_2} D^{(L)*}_{MP}, \tag{A.13}$$

where $R_{l_1Ll_2}$ represents the radial integral for the initial and final states (subsect. 2.2). For the angular distribution, a double sum for the final orbital angular momenta must be considered:

$$W(\vartheta_1) \propto \sum_{M_1M_2Sl_2l_2^*P} |Q_{M_1M_2P}(l_2\, l_2^*)|^2. \tag{A.14}$$

However, since

$$\sum_{M_1} (l_2\, MSM_1|J_2\, M+M_1)(l_2^*\, MSM_1|J_2\, M+M_1) \propto \delta_{l_2 l_2^*}, \tag{A.15}$$

† If the tables of Sharp *et al.* [46]) are used, a factor i^k has to be included in eq. (A.12).

the angular distribution is described, within the present model, as an incoherent sum of the individual components $W_{l_2}(\vartheta_1)$ [eq. (A.12)]:

$$W(\vartheta_1) = \sum_{l_2} z(l_2) W_{l_2}(\vartheta_1). \tag{A.16}$$

The weighting factors $z(l_2)$ can be extracted from the experimental data (subsect. 2.3.1).

If the direct-capture transition to a final state with unique orbital angular momentum l_2 can proceed from several initial partial waves l_1 via the emission of different orders of electric multipole transitions (LM), interference terms in the final angular distributions have to be considered. The wave function for the initial state including the radial dependence is given by (eq. (5)):

$$|J_1 M_1\rangle \propto \sum_{S_1 l_1} \hat{l}_1 \, i^{l_1} \exp(i\varphi_{l_1}) \frac{u_{l_1}(k_1 r)}{k_1 r} \mathscr{Y}^0_{l_1}(\vartheta, \varphi) \chi^{M_1}_{S_1}, \tag{A.17}$$

with

$$\varphi_{l_1} = \sigma_{l_1} - \sigma_0 + \delta_{l_1}.$$

Similarly to the derivation of eq. (A.7), the transition matrix element is given here by

$$Q_{M_1 M_2 P} \propto \sum_{S l_1} i^{l_1} \exp(i\varphi_{l_1}) a^*_S \hat{L} \hat{l}_1^2 \hat{l}_2^{-1} (l_2 M_2 - M_1 S M_1 | J_2 M_2) \times (l_1 0 L 0 | l_2 0)(l_1 0 L M | l_2 M) R_{l_1 L l_2} D^{(L)*}_{MP}, \tag{A.18}$$

where $R_{l_1 L l_2}$ represents the radial integral for the initial and final states (subsect. 2.2). The resultant angular distribution is then given by the sum of the individual angular distributions (eq. (A.12)) and the interference terms:

$$W(\vartheta_1) = \sum_{l_1 L} W_{l_1 L l_2}(\vartheta_1). \tag{A.19}$$

The interference term is given, as usual, by twice the real part of the squared transition matrix element:

$$W_{l_1 L l_2 l^*_1 L^* l_2}(\vartheta_1) = 2 \cos(\varphi_{l_1} - \varphi_{l^*_1}) (-)^{l^*_1 + L^* + l_2} \times \sum_k (l_1 0 l^*_1 0 | k 0) \bar{Z}_1(l_1 L l^*_1 L^*; l_2 k) P_k(\vartheta_1). \tag{A.20}$$

The contributions of the individual components to $W(\vartheta_1)$ depend on the radial matrix element, i.e. on the relative cross sections, which can be obtained from the model calculations (subsect. 2.3.1).

The most frequent type of interference to occur is that between E1 transitions from two initial partial waves l_1 and (l_1+2) to a final orbit l_2. In this case, only a $k = 2$ interference term occurs. Under certain conditions (subsect. 2.1), E1/E2 or E1/M1 types of interference will also be important.

A.1.3. M1 direct-capture transitions. The interaction multipole operator for M1 transitions can be separated into an orbital and a spin part:

$$T_{LM}(\mathrm{M1}) \propto \frac{\hbar}{2mc}\, \boldsymbol{l} + g_t \boldsymbol{s}_t + g_p \boldsymbol{s}_p, \tag{A.21}$$

where $\boldsymbol{S}_t(g_t)$ and $\boldsymbol{S}_p(g_p)$ represent the intrinsic spin (gyromagnetic ratio) of the target nucleus and projectile, respectively. The contribution of the orbital part to the angular distribution is then given by

$$W_{\mathrm{orbital}}(\vartheta_1) = \sum_k (l_1\, 0 l_1\, 0|k0)\bar{Z}_1(l_1\, 1 l_1\, 1;\, l_2\, k) P_k(\vartheta_1). \tag{A.22}$$

The contribution of the spin part to the angular distribution can be calculated in a fashion similar to that given above, but the expression cannot be reduced to a compact form and therefore will not be given here. However there are situations where the angular distribution is given solely by the orbital part ($\boldsymbol{S}_t = \boldsymbol{S}_p = 0$).

A.1.4. The j-dependent nuclear phases. It was assumed above that the nuclear phases δ_{l_1} are j-independent. This is approximately justified if the direct-capture experiments are performed at energies far away from resonances in the reaction. If there are, however, distant resonances with non-negligible resonance tails at the chosen beam energy, the above condition is no longer justified. If, for simplicity, single-valued orbital momenta are assumed, the initial wave function in this case is given [16]) by

$$|\mathrm{i}\rangle \propto \sum_{J_1 M_1} g_{J_1 M_1}(k_1 r)(l_1\, 0 S M_1|J_1\, M_1) \sum_{m_{l_1}\gamma} (l_1\, m_{l_1}\, S_1\, \gamma|J_1\, M_1)\mathscr{Y}_{l_1}^{m_{l_1}} \chi_{S_1}^{\gamma}, \tag{A.23}$$

where the radial wave function is

$$g_{J_1 M_1}(k_1 r) = \frac{1}{k_1 r}\left[F_{l_1}(k_1 r) + \exp(i\delta_{J_1 l_1}) \sin \delta_{J_1 l_1}\{G_{l_1}(k_1 r) + iF_{l_1}(k_1 r)\}\right]. \tag{A.24}$$

The electric transition matrix element now becomes

$$Q_{M_1 M_2 P} \propto (l_1\, 0 L 0|l_2\, 0) \sum_{S J_1 M_1} a_S R(J_1\, l_1) W(L l_2 J_1 S;\, l_1 J_2) \times (L\, M_1 - M_2\, J_2\, M_2|J_1\, M_1)(l_1\, 0 S M_1|J_1\, M_1) D_{MP}^{(L)*}, \tag{A.25}$$

where $R(J_1 l_1)$ represents now the J_1-dependent radial integral. The final expression for the angular distribution is found to be

$$W(\vartheta_1) = \sum_{k S J_1 J_1^*} |a_S|^2 R(J_1\, l_1) R(J_1^*\, l_1) W(L l_2 J_1 S;\, l_1 J_2) W(L l_2 J_1^* S;\, l_1 J_2) \times \bar{Z}(l_1 J_1 l_1 J_1^*;\, S k)\bar{Z}_1(L J_1 L J_1^*;\, J_2\, k) P_k(\vartheta_1), \tag{A.26}$$

where the notation is the same as in ref. [26]). The nuclear phase shifts can be obtained, for example, from a phase shift analysis of elastic scattering data and hence the radial matrix elements can be evaluated. It should be noted that observed angular distri-

butions of the type $\sin^2\vartheta$ represent a clear sign of the absence of j-dependent nuclear phase shifts.

A.2. ANGULAR DISTRIBUTIONS FOR SECONDARY TRANSITIONS

The angular distribution of a secondary γ-ray transition $(L_2\mu_2)$ in the γ-γ cascade between the states $|J_1M_1\rangle \to |J_2M_2\rangle \to |J_3M_3\rangle$ with the primary γ-ray transition $(L_1\mu_1)$ unobserved is given [27]) by

$$W(\vartheta_2) \propto \int \mathrm{d}\Omega_1 \sum_{M_1M_3P_1P_2} \Big| \sum_{\mu_1\mu_2M_2} \langle J_2M_2|T_{L_1\mu_1}|J_1M_1\rangle D^{(L_1)*}_{\mu_1P_1}(\vartheta_1, \varphi_1, 0) \times \langle J_3M_3|T_{L_2\mu_2}|J_2M_2\rangle D^{(L_2)*}_{\mu_2P_2}(\vartheta_2, \varphi_2, 0)\Big|^2, \quad (A.27)$$

which, after integration, reduces [27]) to

$$W(\vartheta_2) \propto \sum_{M_1M_2M_3\mu_1\mu_2P_2} |\langle J_2M_2|T_{L_1\mu_1}|J_1M_1\rangle\langle J_3M_3|T_{L_2\mu_2}|J_2M_2\rangle D^{(L_2)*}_{\mu_2P_2}(\vartheta_2, \varphi_2, 0)|^2. \quad (A.28)$$

In the present case, the primary transition arises from the direct-capture process and the wave functions of the first two states are given by the model (eqs. (5) and (6)), thus the first matrix element can be obtained from eq. (A.7):

$$\langle J_2M_2|T_{L_1\mu_1}|J_1M_1\rangle \propto (l_2\mu_1SM_1|J_2M_2)(l_10L_10|l_20)(l_10L_1\mu_1|l_2\mu_1). \quad (A.29)$$

With the use of the Wigner-Eckart theorem, the second matrix element becomes

$$\langle J_3M_3|T_{L_2\mu_2}|J_2M_2\rangle = (J_2M_2L_2\mu_2|J_3M_3)\langle J_3||T_{L_2}||J_2\rangle. \quad (A.30)$$

The angular distribution can therefore be written as

$$W(\vartheta_2) \propto \sum_{M_1M_2M_3\mu_1\mu_2} (l_2\mu_1SM_1|J_2M_2)^2(l_10L_10|l_20)^2(l_10L_1\mu_1|l_2\mu_1)^2 \times (J_2M_2L_2\mu_2|J_3M_3)^2(L_21L_2\,-1|k0)(L_2\mu_2L_2\,-\mu_2|k0)P_k(\vartheta_2). \quad (A.31)$$

The summation over the magnetic indices can be performed with the help of the usual relations between CG and Racah coefficients and results in

$$W(\vartheta_2) = \sum_k (l_10l_10|k0)W(l_1l_2l_1l_2; L_1k) \times W(J_2l_2J_2l_2; Sk)\bar{Z}_1(L_2J_2L_2J_2; J_3k)P_k(\vartheta_2). \quad (A.32)$$

In the case of a mixture of (L_2, L_2^*) multipoles in the secondary transition, it is straightforward to generalize the above expression to that given in subsect. 2.3.2 (eq. (14)). If the direct-capture transition (unobserved primary) can proceed from several partial waves l_1 to several orbits l_2 in the intermediate state, then the final angular distribution for the secondary transition is given by an incoherent sum over the individual components:

$$W(\vartheta_2) = \sum_{l_1l_2} \sigma_{l_1l_2} W_{l_1l_2}(\vartheta_2), \quad (A.33)$$

where the weighting factors $\sigma_{l_1 l_2}$ can be obtained either from the primary transitions or from direct-capture model calculations.

The γ-ray angular distribution for the nth secondary transition can be calculated with the help of an extended ansatz (A.27):

$$W(\vartheta_n) \propto \sum_k (l_1 0 l_1 0|k0) W(l_1 l_2 l_1 l_2; L_1 k) \times W(J_2 l_2 J_2 l_2; Sk) W(J_2 J_3 J_2 J_3; L_2 k) \ldots W(J_{n-1} J_n J_{n-1} J_n; L_{n-1} k) \times \bar{Z}_1(L_n J_n L_n J_n; J_{n+1} k) P_k(\vartheta_n). \quad \text{(A.34)}$$

If the mth intermediate (unobserved) transition is composed of two multipoles $(L_m L_m^*)$, then the appropriate Racah coefficient has to be replaced as usual [27]) by

$$W(J_m J_{m+1} J_m J_{m+1}; L_m k) + \delta^2 W(J_m J_{m+1} J_m J_{m+1}; L_m^* k), \quad \text{(A.35)}$$

where δ is the multipole mixing ratio.

A.3. INTERFERENCE BETWEEN DIRECT CAPTURE AND RESONANT TRANSITIONS

The excitation function of a γ-ray transition which contains contributions from the direct-capture process as well as from a resonance state is given by

$$\sigma(E, \vartheta) \propto \sum_{M_1 M_3 P_R P_D} \Big| \sum_{M_2 M_R M_D} \{\langle J_3 M_3 | T_{L_R M_R} | J_2 M_2 \rangle \langle J_2 M_2 | T_{l_R 0} | J_1 M_1 \rangle D^{(L_R)*}_{M_R P_R}(\vartheta, \varphi, 0) + \langle J_3 M_3 | T_{L_D M_D} | J_1 M_1 \rangle D^{(L_D)*}_{M_D P_D}(\vartheta, \varphi, 0)\}|^2, \quad \text{(A.36)}$$

where J_1 and J_3 are the spins of the initial (channel spin state $\boldsymbol{J}_1 = \boldsymbol{j}_t + \boldsymbol{j}_p$) and final states, respectively, and J_2 is the spin of the resonance state. The latter state is formed by partial l_R wave capture ($\boldsymbol{J}_2 = \boldsymbol{l}_R + \boldsymbol{J}_1$). The indices R and D refer to resonance and direct capture, respectively. This expression can be reduced to

$$\sigma(E, \vartheta) = \sigma_R(E) W_R(\vartheta) + \sigma_D(E) W_D(\vartheta) + 2\sqrt{\sigma_R(E)\sigma_D(E)} \cos(\varphi_R - \varphi_D) W^{\text{int}}_{R,D}(\vartheta), \quad \text{(A.37)}$$

where the resonance cross section $\sigma_R(E)$, the γ-ray angular distribution of the resonance transition $W_R(\vartheta)$ and the resonance phase shifts φ_R are given by refs. [26, 27]). The corresponding expressions for the direct capture process have been described in previous subsections. The interference term $W^{\text{int}}_{R,D}(\vartheta)$ is found to be

$$W^{\text{int}}_{R,D}(\vartheta) = (-)^P \hat{J}_2 \hat{l}_f W(l_R L_R J_1 J_3; l_f J_2) \sum_k (l_R 0 l_D 0|k0) \bar{Z}_1(l_R L_R l_D L_D; l_f k) P_k(\vartheta), \quad \text{(A.38)}$$

where the phase P is given by

$$P = J_2 + J_3 + l_R + l_D + L_D + \tfrac{1}{2}(l_D + l_R + L_D + L_R) + P_{L_D L_R}, \quad \text{(A.39)}$$

with $P_{L_D L_R} = L_D$, $L_D + \frac{3}{2}$, $\frac{1}{2}$ and 0 for (EL_D, EL_R), (EL_D, ML_R), (ML_D, EL_R) and (ML_D, ML_R) interfering multipole transitions, respectively. The quantum numbers l_D and l_f denote the orbital angular momenta involved in the direct-capture process (sect. 2).

References

1) W. A. Fowler, C. C. Lauritsen and A. V. Tollestrup, Phys. Rev. **76** (1949) 1767
2) D. H. Wilkinson, Phil. Mag. **43** (1952) 659
3) G. M. Griffiths, E. A. Larson and L. P. Robertson, Can. J. Phys. **40** (1962) 402
4) J. B. Warren *et al.*, Can. J. Phys. **32** (1954) 563
5) R. A. Laubenstein and M. J. W. Laubenstein, Phys. Rev. **84** (1951) 18
6) N. W. Tanner, Phys. Rev. **114** (1959) 1060
7) J. J. Domingo, Nucl. Phys. **61** (1965) 39
8) H. H. Woodbury, A. V. Tollestrup and R. B. Day, Phys. Rev. **93** (1954) 1311
9) W. Trost, Thesis, Universität Freiburg, 1963
10) W. Trost, H. J. Rose and F. Riess, Phys. Lett. **10** (1964) 83
11) G. M. Bailey and D. F. Hebbard, Nucl. Phys. **46** (1963) 529, **49** (1963) 666
12) R. P. Kavanagh, Nucl. Phys. **15** (1960) 411
13) J. B. Warren, T. K. Alexander and G. B. Chadwick, Phys. Rev. **101** (1956) 242
14) S. L. Blatt *et al.*, Phys. Rev. **176** (1968) 1147
15) P. D. Parker and R. W. Kavanagh, Phys. Rev. **131** (1963) 2578
16) R. F. Christy and I. Duck, Nucl. Phys. **24** (1961) 89
17) T. A. Tombrello and P. D. Parker, Phys. Rev. **131** (1963) 2582
18) R. G. Thomas, Phys. Rev. **84** (1951) 1061
19) G. M. Bailey, G. M. Griffiths and T. W. Donnelly, Nucl. Phys. **A94** (1967) 502
20) T. W. Donnelly, thesis, University of British Columbia, 1967
21) A. Faessler, Nucl. Phys. **65** (1965) 329
22) W. J. Thompson, Phys. Lett. **28B** (1968) 324
23) A. M. Lane, Nucl. Phys. **11** (1959) 625
24) A. M. Lane and J. E. Lynn, Nucl. Phys. **11** (1959) 646, **17** (1960) 563
25) H. Morinaga and C. Ishii, Prog. Theor. Phys. **23** (1960) 161
26) A. J. Ferguson, Angular correlation methods in gamma-ray spectroscopy (North-Holland, Amsterdam, 1965)
27) H. J. Rose and D. M. Brink, Rev. Mod. Phys. **39** (1967) 306
28) S. T. Thornton, Nucl. Phys. **A137** (1969) 531
29) C. J. Oliver *et al.*, Nucl. Phys. **A127** (1969) 567
30) C. Rolfs and A. E. Litherland, Gamma-rays from capture reactions, vol. 7D, ed. J. Cerny (Academic Press, New York, to be published in March 1974)
31) C. Rolfs, A. M. Charlesworth and R. E. Azuma, Nucl. Phys. **A199** (1973) 257
32) C. Rolfs *et al.*, Nucl. Phys. **A199** (1973) 274
33) C. Rolfs *et al.*, Nucl. Phys. **A199** (1973) 289
34) C. Rolfs *et al.*, Nucl. Phys. **A199** (1973) 306
35) C. Rolfs *et al.*, Nucl. Phys. **A199** (1973) 328
36) I. Berka, C. Rolfs and R. E. Azuma, Can. J. Phys. **50** (1972) 1682
37) C. Rolfs, Z. Phys. **249** (1972) 312
38) F. Ajzenberg-Selove, Nucl. Phys. **A166** (1971) 1
39) L. M. Polsky, C. H. Holbrow and R. Middleton, Phys. Rev. **186** (1969) 966
40) J. Millener, Oxford University, private communication
41) T. A. Tombrello and G. C. Phillips, Phys. Rev. **122** (1961) 224
42) R. E. Hester, R. E. Pixley and W. A. S. Lamb, Phys. Rev. **111** (1968) 1604
43) H. G. Benson and B. H. Flowers, Nucl. Phys. **A126** (1969) 332
44) P. J. Ellis and T. Engeland, Nucl. Phys. **A144** (1970) 161, **A181** (1972) 368
45) S. R. Salisbury and H. T. Richards, Phys. Rev. **126** (1962) 2147
46) W. T. Sharp *et al.*, Atomic Energy of Canada, Ltd., CRT-556, AECL-97 (1957)
47) M. Suffert, Proc. panel meeting (IAEA, October 1972)
48) C. Rolfs, Proc. panel meeting (IAEA, October 1972)
49) G. E. Brown, Nucl. Phys. **57** (1964) 339
50) C. F. Clement, A. M. Lane and J. R. Rook, Nucl. Phys. **66** (1965) 273, 293
51) G. Longo and F. Saporetti, Nucl. Phys. **A127** (1969) 503
52) J. P. Boisson and S. Jang, Nucl. Phys. **A189** (1972) 334

53) T. H. Hall, University of British Columbia, private communication
54) W. A. Fowler, G. R. Caughlan and B. A. Zimmermann, Ann. Rev. Astronomy and Astrophysics **5** (1967) 525
55) E. M. Burbridge *et al.*, Rev. Mod. Phys. **29** (1957) 547
56) H. P. Trautvetter and C. Rolfs, Bull. Am. Phys. Soc. **18** (1973) 678
57) C. Rolfs, K. P. Jackson and R. E. Azuma, to be published
58) A. O. Nier, Phys. Rev. **77** (1950) 789
59) F. Ajzenberg-Selove, Nucl. Phys. **A190** (1972) 1
60) R. G. H. Robertson, Phys. Rev. **7** (1973) 543
61) R. E. Brown, Phys. Rev. **125** (1962) 347
62) A. M. Lane, Rev. Mod. Phys. **32** (1960) 520
63) A. Moszkowski, Beta- and gamma-ray spectroscopy, ed. K. Siegbahn (North-Holland, Amsterdam, 1955) p. 373 ff.
64) E. K. Warburton and J. Weneser, Isospin in nuclear physics, ed. D. H. Wilkinson (North-Holland, Amsterdam, 1969) p. 173 ff.
65) E. Vogt, C. Michaud and H. Reeves, Phys. Lett. **19** (1965) 570